Laser-driven single shock compression of fluid deuterium from 45 to 220 GPa

D. G. Hicks,[1,*] T. R. Boehly,[2] P. M. Celliers,[1] J. H. Eggert,[1] S. J. Moon,[1] D. D. Meyerhofer,[2,†] and G. W. Collins[1]
[1]*Lawrence Livermore National Laboratory, Livermore, California 94550, USA*
[2]*Laboratory for Laser Energetics, University of Rochester, Rochester, New York 14623, USA*
(Received 13 May 2008; revised manuscript received 12 August 2008; published 26 January 2009)

The compression (η) of liquid deuterium between 45 and 220 GPa under laser-driven shock loading has been measured using impedance matching to an aluminum (Al) standard. An Al impedance-match model derived from a best fit to absolute Hugoniot data has been used to quantify and minimize the systematic errors caused by uncertainties in the high-pressure Al equation of state. In deuterium below 100 GPa results show that $\eta \simeq 4.2$, in agreement with previous impedance-match data from magnetically driven flyer and convergent-explosive shock wave experiments; between 100 and 220 GPa η reaches a maximum of ~ 5.0, which is less than the sixfold compression observed on the earliest laser-shock experiments but greater than expected from simple extrapolations of lower-pressure data. Previous laser-driven double shock results are found to be in good agreement with these single shock measurements over the entire range under study. Both sets of laser-shock data indicate that deuterium undergoes an abrupt increase in compression at around 110 GPa.

DOI: 10.1103/PhysRevB.79.014112 PACS number(s): 62.50.−p, 64.30.−t

I. INTRODUCTION

The behavior of hydrogen near its metal-insulator transition has long been a source of fundamental scientific interest.[1] Experiments on solid hydrogen show that even at 316 GPa and 13-fold compression the vibron signature of the H_2 molecule persists and hydrogen remains an insulator;[2] evidently such an extreme increase in density alone is insufficient to dissociate this most basic chemical bond. In the fluid, however, metallization occurs at considerably lower densities. At several thousand degrees dense hydrogen transforms into a conducting fluid[3,4] indicating significant dissociation even at only fourfold compression.[4] The behavior of hydrogen near this fluid insulator-to-metal transition has profound implications for the interiors of giant planets[5] and is central to resolving basic questions about planetary formation.[6]

Experimental studies of this complex fluid are accomplished using dynamic compression measurements near 100 GPa. In particular, the compression (η) along the principal Hugoniot of liquid deuterium[7] (D_2) has become the single most important experimental metric by which theories of hydrogen at high temperature and pressure are judged. Chemical free-energy models[8–12] and *ab initio* simulations[13–22] have been used to predict this Hugoniot but results vary widely and span the range between $\eta=4$ and $\eta=6$ at pressures near 100 GPa. The accuracy of these different calculational approaches is seen as a fundamental test of whether traditional chemical models, which are limited by the *a priori* properties assigned to atoms and molecules, can compete with first-principles calculations, which are limited by their numerical approximations.

In an unprecedented comparison, experiments from three different shock wave platforms have been used to measure the deuterium Hugoniot; however, the results have remained inconclusive. Laser-driven measurements[23–25] showed $\sim$6-fold maximum compression between 50 and 320 GPa, magnetically driven flyer experiments[26,27] observed $<$4.4-fold compression up to 100 GPa, and convergent explosive-driven measurements[28–31] found just over fourfold compression near 100 GPa. The laser-driven experiment, which was the only one to use an absolute radiography measurement technique, is thus in disagreement with the other two experiments. Since both magnetic-flyer and convergent-explosive experiments instead used impedance-matching (IM) methods to determine the deuterium Hugoniot, it is imperative to establish whether the difference in measured compression is caused by the drive platforms and their associated time scales or is an artifact of the measurement technique.

To address this question, impedance-matching measurements of the deuterium Hugoniot were made using laser-driven shock waves. Aluminum was chosen as the material standard, as it was for the magnetic- and explosive-driven experiments, because its high-pressure equation of state (EOS) is comparatively well constrained by experimental data. An experimentally based Al Hugoniot is derived and uncertainties in the Hugoniot and release curves are propagated as systematic errors. Such rigorous error analysis is particularly important because of the large impedance mismatch between Al and D_2 which not only magnifies the effect of small Al EOS uncertainties but also necessitates knowing the Al EOS to extremely high pressures where such uncertainties become increasingly significant ($\sim$700 GPa shocks in aluminum are required to generate 100 GPa shocks in deuterium). This experimentally based Al impedance-matching model is found to be critical for accurate analysis of data at D_2 pressures of $\sim$100 GPa and above.

Our results show that between 45 and 101 GPa $\eta \simeq 4.2$, in good agreement with previous magnetic- and explosive-driven impedance-matching measurements. This indicates that the discrepancy between earlier experiments in this range was due to the differences between radiography and impedance-matching measurement techniques and not to any inherent differences between shock platforms. At around 110 GPa, the compression increases sharply to a maximum of $\eta \simeq 5.0$, remaining between 4.5 and fivefold compression up to 220 GPa. This is in excellent agreement with previous laser-driven double shock measurements.[32] Whether or not

this abrupt increase in compression near 110 GPa is evidence of a phase transition, or perhaps a nearby critical point, is discussed.

This paper is organized as follows: In Sec. II previous theoretical and experimental work is reviewed. In Sec. III details of the experimental setup and diagnostics are described. Section IV discusses the aluminum impedance-matching model and propagation of systematic uncertainties, as well as how to account for different initial densities when comparing results from different experiments. In Sec. V the results for the experimental observables are presented along with the inferred principal Hugoniot. In Sec. VI previous double shock and reverberation time data are compared to the single shock results, with conclusions and discussion presented in Sec. VII.

II. BACKGROUND

A. Theoretical models

There is a diverse array of calculations for the deuterium Hugoniot in the neighborhood of 100 GPa, providing a clear comparison among a wide variety of theoretical approaches (see Fig. 1). These various models can be divided roughly into two categories: (1) analytical-based or chemical models, which legislate the properties of atoms, molecules, electrons, and ions based on our common notions of each and (2) *ab initio* models, which assume the properties of electrons and nuclei only and do not explicitly define higher-level complexes (e.g., atoms or molecules) as distinguishable entities. *Ab initio* models, being based on large numerical first-principles simulations, have the potential for revealing fundamentally new entities but ultimately cover a limited phase space and often provide less physical intuition than do the simpler chemical models. Hydrogen has thus become a testing ground for these competing conceptual frameworks.

Over the years, several chemical models, typically applying perturbation theories for the dense molecular-atomic fluid, have been shown to predict anywhere between fourfold and sixfold compressions in deuterium at 100 GPa. The earliest widely used chemical model was that by Kerley,[8] referred to here as the Sesame72 model. This multiphase multicomponent EOS included dissociation and ionization and combined molecular and atomic fluid phases using the linear-mixing approximation. With no experimental guidance this model predicted $\eta=4$ at 100 GPa, increasing slightly at higher pressures. Much later, a model by Ross[10] applied a linear-mixing rule to interpolate between the low-pressure soft sphere molecular fluid EOS and the high-pressure one-component plasma. Adjusting a free-energy correction to match lower-pressure reflected shock temperature measurements[33] caused significant softening, giving $\eta_{\max}=6.0$ at 90 GPa. Today these two models, which preceded any measurements in the 100 GPa regime, are generally regarded to be extrema bounding the region of validity, with the Sesame72 model considered "stiff" and the Ross model considered "soft." Most models predict compressions that lie in between. Other analytical-based models include Kerley's improved models, the most recent of which is referred to here as Kerley03,[34] the wide-ranging EOS by Saumon,[9] another fluid variational model,[12] and the high-temperature dense plasma activity expansion model (ACTEX).[11]

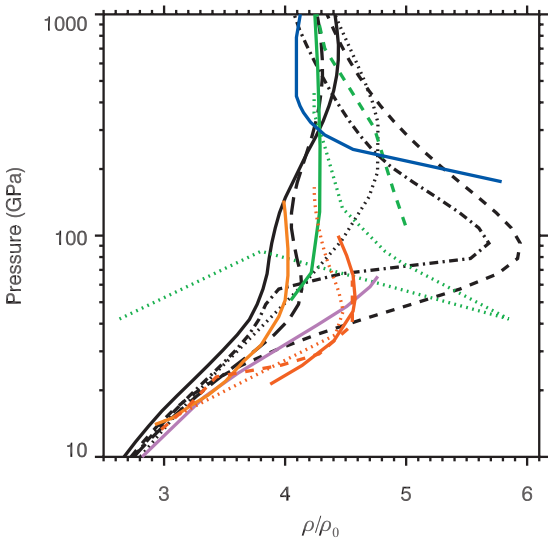

FIG. 1. (Color) An assortment of calculated single shock principal Hugoniots for D_2 starting from the initial density of 0.171 g/cm^3. The different theoretical approaches are distinguished by color: (a) Free-energy models from Saumon and Chabrier (Ref. 9) developed for astrophysical calculations (dotted-dashed black curve), an early table from the Sesame database by Kerley (Sesame72) (Ref. 8) (solid black curve), an updated EOS from Kerley (Ref. 34) (long-dashed black curve), a linear-mixing model from Ross (Ref. 10) (dashed black curve), and the original solid-to-plasma interpolation model (qEOS) by More *et al.* (Ref. 66) (dotted black curve); (b) restricted PIMC simulations by Magro *et al.* (Ref. 19) (dotted green curve) and Militzer and Ceperley (Ref. 20) (solid green curve), and direct PIMC by Bezkrovniy *et al.* (Ref. 21) (dashed green curve); (c) reaction Ensemble Monte Carlo technique (Ref. 21) (solid pink curve); (d) DFT calculations by Collins *et al.* (Ref. 16) (solid red curve), Desjarlais (Ref. 17) (dotted red curve), and Bonev *et al.* (Ref. 18) (dashed red curve); (e) Tight-binding calculations by Lenosky *et al.* (Ref. 13) (solid orange curve); and (f) activity expansion (ACTEX) predictions by Rogers (Ref. 11) (solid blue curve).

Ab initio methods also exhibit a wide range of predictions for the deuterium Hugoniot. Although termed "*ab initio*" or "first-principles" methods, these techniques all implement different approximations to make the problem numerically tractable. The proliferation of these methods and their different predictions for the deuterium Hugoniot provide a useful window into the validity of these various approximations. Tight-binding[13] and density-functional theory (DFT) molecular-dynamics[14–18] methods have been used to calculate the Hugoniot below ~100 Gpa. Tight-binding calculations show $\eta_{\max}=4$ near 50 GPa; DFT methods show $\eta_{\max}=4.3-4.5$ around 50 GPa. Initial disagreement between DFT calculations[14–16] and low-pressure gas gun results[35] was later rectified.[17,18] Path integral Monte Carlo (PIMC) methods, in contrast, have been used to calculate the Hugoniot above ~100 GPa. Restricted PIMC found either $\eta_{\max}=6$ using the nodes of the free particle density matrix[19] or $\eta_{\max}=4.3$ using those from the variational density matrices.[20] The direct PIMC (Refs. 21 and 22) approach, which avoids such path

integral restrictions, found $\eta=5$ near 100 GPa. Another approach, using an electron force field method, also predicted $\eta=5$ between 100 and 200 GPa.[36]

These different results demonstrate the challenges of modeling hydrogen near the fluid metal-insulator transition. Hydrogen at 100 GPa lies at the high-temperature limit of available DFT calculations, the low-temperature limit of PIMC calculations, and in between the asymptotic ideal limits of chemical models. Experiments in this regime are thus crucial to establishing the ultimate limitations of these different theoretical paradigms.

B. Previous experiments

Until 1997, the highest pressures achieved in liquid deuterium had been attained on gas gun experiments.[35,37,38] These experiments used impedance matching to an aluminum standard and reached a maximum single shock pressure of 25 GPa. Experiments around 100 GPa were pioneered by workers using laser-driven shock waves[23–25] and followed soon thereafter by experiments using magnetically driven flyers[26,27] and convergent explosives.[28–31] These experiments used either one of the two fundamentally different measurement techniques: the laser-shock studies used x-ray radiography while the other two experiments both used impedance matching to aluminum.

The laser-driven shock measurements, performed on the Nova facility,[23–25] employed time-resolved x-ray radiography to directly measure both shock and particle speeds, thus obtaining a model-independent measurement of the deuterium compressibility. Such an approach was taken because of the unavailability of accurate high-pressure impedance-matching standards at the time. Measurements observed $\eta\sim 5.5-6.0$ from 50 to 320 GPa. Thus far such high compressions have not been reproduced elsewhere, although the radiography method has yet to be repeated on deuterium.

The second set of experiments used flyer plates magnetically driven by the Z machine to generate shocks up to 101 GPa. By applying the impedance-matching technique with aluminum as the standard, Knudson *et al.*[26,27] found $\eta\simeq 4.3$ at 40 GPa, stiffening to $\eta\simeq 4$ at 101 GPa. Importantly, Knudson *et al.*[39,40] performed near-absolute and absolute measurements of the aluminum Hugoniot and release to establish their standard in the relevant pressure range.

Finally, explosively driven experiments in convergent geometry were performed on initially solid,[28,29] gaseous,[30] and liquid[31] deuterium also using aluminum impedance matching. Applying the necessary corrections to account for initial density differences,[41] these data indicate that $\eta\simeq 4.0-4.5$ below 107 GPa.

Multiple shock experiments have also been studied extensively and provide additional constraints on the deuterium EOS. Although early laser-driven double shock measurements on the Nike laser[42,43] using an aluminum anvil appeared to be consistent with a soft EOS, subsequent higher precision double shock data obtained on the Omega laser[32] using a quartz anvil indicated a stiff EOS for first-shock pressures below ~100 GPa and above ~200 GPa, and an "intermediate" EOS suggestive of $\eta\sim 5$ in between. The Omega experiments provide a rigorous test of the deuterium compressibility (albeit in the double shock state) because the data are independent of models for the standard. Magnetic-flyer-driven double shock compression[27] and multiple shock reverberation[27,44] experiments indicated a stiff EOS up to 100 GPa, in agreement with the Omega laser-driven double shock measurements.[32] Double shock measurements on different platforms are thus in agreement, at least over the pressure range where they can be compared directly.

Although much has been made of the disagreement between single shock experiments from different platforms, it is worth noting that these experiments can only be compared over a relatively limited pressure range. The magnetic-flyer and convergent-explosive data reach just over 100 GPa while the Nova data extend to 340 GPa. Thus the only pressure range over which all data can be compared directly is around 100 GPa and below.

III. EXPERIMENTAL METHOD

The experiment described in this paper was performed on the Omega laser at the University of Rochester, a neodymium-doped phosphate glass system operating with frequency-tripled 0.35 μm light.[45] To generate the shock pressures explored in these experiments, laser energies up to 3 kJ were delivered using a nominally square pulse 3.7 ns in duration. The laser focal region was smoothed using distributed phase plates, producing a near uniformly irradiated spot 800 μm in diameter. Targets consisted of a flat diamond-turned aluminum pusher (50 μm or 90 μm thick) attached to a copper cell filled with cryogenic deuterium (see Fig. 2). A 20 μm CH (glow discharge polymer) ablator was used to reduce hard x-ray generation. Preheat affects in these types of targets and with these laser conditions were previously found to be negligible.[32] A z-cut α-quartz "witness plate" was glued over half of the Al pusher as a reference window for determining the shock velocity immediately prior to breakout from Al (see below). By observing the solid-liquid transition in deuterium and using the properties of deuterium on the saturation line,[46] we determined that the deuterium density was 0.174 g/cm^3. At this density and at the probe laser wavelength of 532 nm, the index of refraction was calculated to be 1.138.[46] At room temperature, the density of quartz was measured to be 2.65 g/cm^3 and the refractive index along its c axis at 532 nm was found to be 1.547. Small changes in the properties of aluminum upon cooling to cryogenic temperatures were taken into account; changes in quartz properties were found to be insignificant.[47]

Shock velocities were determined using a line-imaging velocity interferometer system for any reflector (VISAR) (Refs. 48–51) which measures the Doppler shift of a moving reflector. At the high pressures involved in these experiments, shock waves in the initially transparent quartz[52] and deuterium[4] are reflecting. Thus the VISAR directly measures the shock front velocity in both materials. Two VISARs with different velocity sensitivities were used to resolve 2π phase shift ambiguities which occur at shock breakout. The velocity sensitivities for the two VISAR instruments were 6.069 and 14.138 μm/ns per fringe for deuterium and 4.465 and

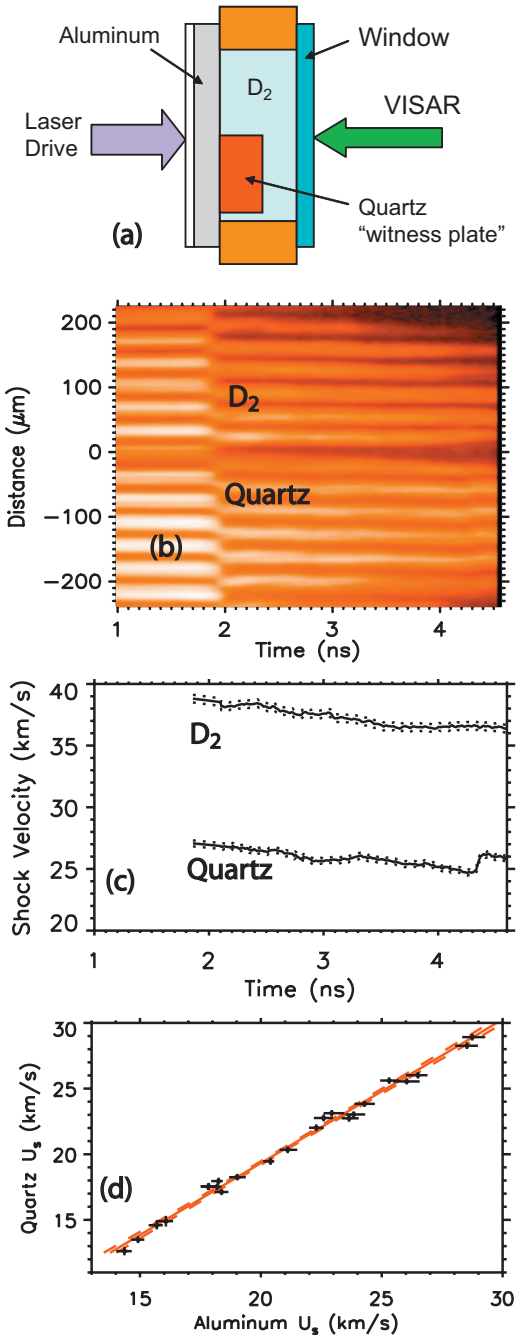

FIG. 2. (Color) (a) Sketch of the target used for single shock measurements. (b) A line VISAR data record showing simultaneous shocks in D_2 and quartz. (c) Sample shock velocity history in deuterium and quartz with dotted lines representing measurement errors. The shock velocity in aluminum immediately *before* breakout is then determined from the measured shock velocity in quartz immediately *after* breakout using the previously determined experimental fit shown in (d) (Ref. 53).

10.400 μm/ns per fringe for quartz. Postprocessing of the VISAR images using Fourier transform methods determines the fringe position to $\lesssim$5% of a fringe; the resulting velocities are measured to around 1% precision since shock speeds are high enough to cause multiple fringe shifts. The probe source was an injection-seeded Q-switched yttrium-aluminum garnet laser, operating at a wavelength of 532 nm with a pulse length of $\sim$25 ns. Streak cameras with temporal windows of between 3 and 10 ns were used to detect the reflected probe signal. The time resolution of the VISAR and streak camera system was $\sim$40 ps.

Shock velocities in aluminum ($U_{s\mathrm{Al}}$) and deuterium ($U_{s\mathrm{D}}$) represent the primary experimental observables for the impedance-matching calculations. These velocities must be taken immediately before and after the shock wave crosses the Al-D_2 interface for the impedance-matching condition to apply; otherwise, corrections must be made for shock unsteadiness effects as was done in the experiments using the unsteady convergent geometry.[28–31] To address this issue, we developed an approach[53] to measure both $U_{s\mathrm{Al}}$ and $U_{s\mathrm{D}}$ at shock breakout using the continuous time-resolved readout provided by the VISAR combined with a quartz witness plate mounted on the Al pusher [see Fig. 2(a)]. The VISAR simultaneously measures both the quartz ($U_{s\mathrm{Q}}$) and deuterium ($U_{s\mathrm{D}}$) shock velocities at breakout from the aluminum [see Figs. 2(b) and 2(c)]; subsequent unsteadiness in the shock velocities does not affect the results since it is only the velocity at breakout that is required (shock accelerations at breakout varied between −0.2 and −4.2 km/s ns). Then, using the previously established relationship [see Fig. 2(d) and discussion below], $U_{s\mathrm{Al}}$ is determined directly from the measured $U_{s\mathrm{Q}}$. This provides an entirely VISAR-based impedance-matching measurement and avoids the larger errors typically incurred by a transit time measurement. In these single shock measurements there is no need to use EOS models or hydrodynamic codes to correct the observables, as was done to account for the density profile of the Al flyer in the magnetic-flyer experiments,[26,27] or the shock steadiness and curvature effects, as was done in the convergent geometry experiments.[28–31]

The linear relationship between $U_{s\mathrm{Al}}$ and $U_{s\mathrm{Q}}$ was established in a previous set of experiments[53] for the range $200 < P_{\mathrm{Q}} < 1500$ GPa, as shown in Fig. 2(d). The Al-quartz data were best fit with $U_{s\mathrm{Al}} = a_0 + a_1(U_{s\mathrm{Q}} - \beta)$, where $\beta = 20.57$, $a_0 = 21.14$ km/s, and $a_1 = 0.91$. The uncertainty in this fit is given by $\delta U_{s\mathrm{Al}} = [\sigma_{a0}^2 + (U_{s\mathrm{Q}} - \beta)^2\sigma_{a1}^2 + a_1^2\delta U_{s\mathrm{Q}}^2]^{1/2}$, where $\sigma_{a0} = 0.12$, $\sigma_{a1} = 0.03$, and $\delta U_{s\mathrm{Q}}$ is typically $\sim$1%. The resulting $\delta U_{s\mathrm{Al}}$ is also $\sim$1% because the uncertainty of the linear fit (over 23 data points) is significantly less than the uncertainty of a single data point. It is important to emphasize that the quartz thus serves only as a calibrated gauge; no details about its high-pressure properties (such as its release behavior) are required beyond this correlation between single shock velocities in aluminum and quartz.

IV. DATA REDUCTION

A. Impedance-match analysis

IM (Refs. 54 and 55) is the calculational procedure used to extract the deuterium particle velocity ($U_{p\mathrm{D}}$), pressure (P_{D}), and compression (η_{D}) from the experimental observables: $U_{s\mathrm{Al}}$ and $U_{s\mathrm{D}}$. This requires knowing both the principal Hugoniot and the release curves of the standard material (Al). We have constructed an IM method using a best fit to high-pressure Al data which allows errors in both the Hugo-

niot and the release curves to be calculated independently and propagated through the analysis. Although a full explanation of this method was given in an earlier paper,[56] many of the essential details will be repeated in this section, focusing on the implications for D_2. The approach is similar in essence to the one developed by Nellis and Mitchell[57] in that absolute (model-independent) Hugoniot data were used to derive the Al Hugoniot while release curves were constructed in a way that depended minimally on theoretical models.

The first step in developing our IM model was to establish the principal Hugoniot for aluminum. To do this we represented the Hugoniot by a best fit to available absolute Al Hugoniot data up to 3000 GPa. These reference data included the accurate experiments of Al'tshuler *et al.*,[58] Mitchell and Nellis,[59] Knudson *et al.*,[39] Simonenko *et al.*,[60] and Podurets *et al.*[61] as well as additional unpublished data from Knudson.[62] Our U_s-U_p fit employed a weighted χ^2 minimization of a piecewise linear form selected from among a number of choices using standard statistical F-test methods. It is given by $U_{s\mathrm{Al}}=(9.449\pm0.020)+(1.324\pm0.016)(U_{p\mathrm{Al}}-3.0220)$ for $U_{p\mathrm{Al}}\leq 6.763$ and $U_{s\mathrm{Al}}=(17.992\pm0.078)+(1.167\pm0.026)(U_{p\mathrm{Al}}-9.8381)$ for $6.762<U_{p\mathrm{Al}}\leq 30$, where all values are given in km/s. In the high-pressure range very similar fits have been reported by Trunin.[63] Small changes to this fit due to operation at cryogenic temperatures were taken into account.[47]

As was shown previously (see Fig. 4 of Ref. 56), the various commonly available Al EOS models typically pass through the error bars of individual measurements but in general were slightly stiffer than the best fit given above. Particularly stiff was the EOS table used in the analysis of the magnetic-flyer experiments (the 3700 table from Kerley[64]) whose validity was verified by Hugoniot[39] and release[40] measurements only up to 500 GPa. This table predicted a Hugoniot that fell outside the 1σ uncertainty band of the best fit experimental Hugoniot above $P_{\mathrm{Al}}=450$ and out of the 2σ band above 630 GPa. The use of this particular EOS for the higher-pressure data we have in this experiment (where Al pressures reach a maximum of ~1400 GPa) would result in significant error.

The second step in developing the aluminum IM model was to establish the release behavior. In order to minimize the influence of theoretical input only the difference of the release curves from the reflected principal Hugoniot (in the P-U_p plane) was calculated. Previously, Gruneisen parameters were used to determine this.[57] Our approach was to calculate the difference by averaging predictions from several available Al EOS models (Sesame[65] Tables 3713, 3715, and 3719, Kerley's 3700 table,[64] and qEOS[66]), with the resulting standard deviation being *defined* as the systematic uncertainty in the release.[56] This level of model-dependent input was unavoidable and ranged from 2% to 4% of the final pressure, with an uncertainty in the fit of $\pm(1.4-1.6)\%$. These release curve calculations are in good agreement with the release measurements of Holmes[67] and Knudson *et al.*[40] (see Fig. 7 of Ref. 56). Importantly, the uncertainties in those measurements are comparable to our calculated systematic errors; this provides confidence in our systematic error analysis.

The resulting systematic uncertainties in the release velocity $U_{p\mathrm{D}}$ are shown in Fig. 3 as a function of final D_2 shock pressure for a set of synthetic shock data calculated from theoretical models. The dashed curves show the contribution from the Hugoniot uncertainty, the dotted curves show the contribution from the release profile uncertainty, and the total systematic uncertainty (quadrature sum) is shown as the solid curves; all curves are labeled as "K" or "R" corresponding, respectively, to the Sesame72 (by Kerley) or Ross EOS models. The Hugoniot uncertainty contribution has a local maximum near 40 GPa originating from increased fitting uncertainties near the connection between the piecewise segments of the low- and high-pressure fits of the Hugoniot (270 GPa along the Al Hugoniot). There is also a maximum in the release profile uncertainty near 50 GPa which arises because of large variations among the various Al models near the Al melt transition. For D_2 pressures $\gtrsim$100 GPa the systematic uncertainty is ~1.5% and shows no unusual behavior because the Al states are on the high-pressure branch of the Hugoniot and well above the melt transition.

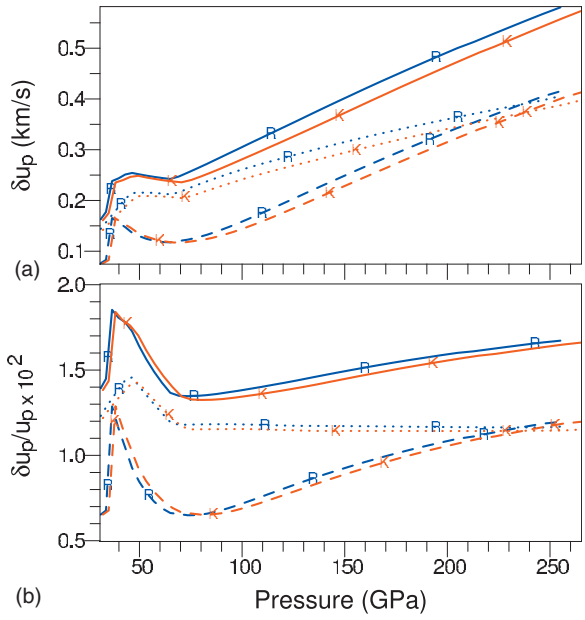

FIG. 3. (Color) Systematic uncertainties in the deuterium particle velocity arising from uncertainties in the aluminum Hugoniot and release, shown as a function of deuterium shock pressure. (a) Magnitude of the total systematic uncertainty (solid curves) computed from the quadrature sum of contributions from the uncertainty in the Hugoniot (dashed curves) and uncertainty in the release (dotted curves). The total systematic uncertainty depends only slightly on the D_2 EOS: Errors shown were calculated using either the Sesame72 EOS table (red) or the Ross linear-mixing EOS (blue). (b) A similar plot showing the relative magnitude of the systematic uncertainties.

Figure 4 shows an example impedance-match calculation for deuterium at 80 GPa which includes the random uncertainties (from $U_{s\mathrm{Al}}$ and $U_{s\mathrm{D}}$) and the systematic uncertainties from both the Hugoniot and release portions of the IM calculations. Systematic and random errors in $U_{p\mathrm{D}}$, P_{D}, and ρ_{D} are given separately in Table I.

Over a broad range of final D_2 pressures (from 50 to 250 GPa) systematic uncertainties from the Al EOS are thus ~1.5% of U_p and are essentially independent of whether the

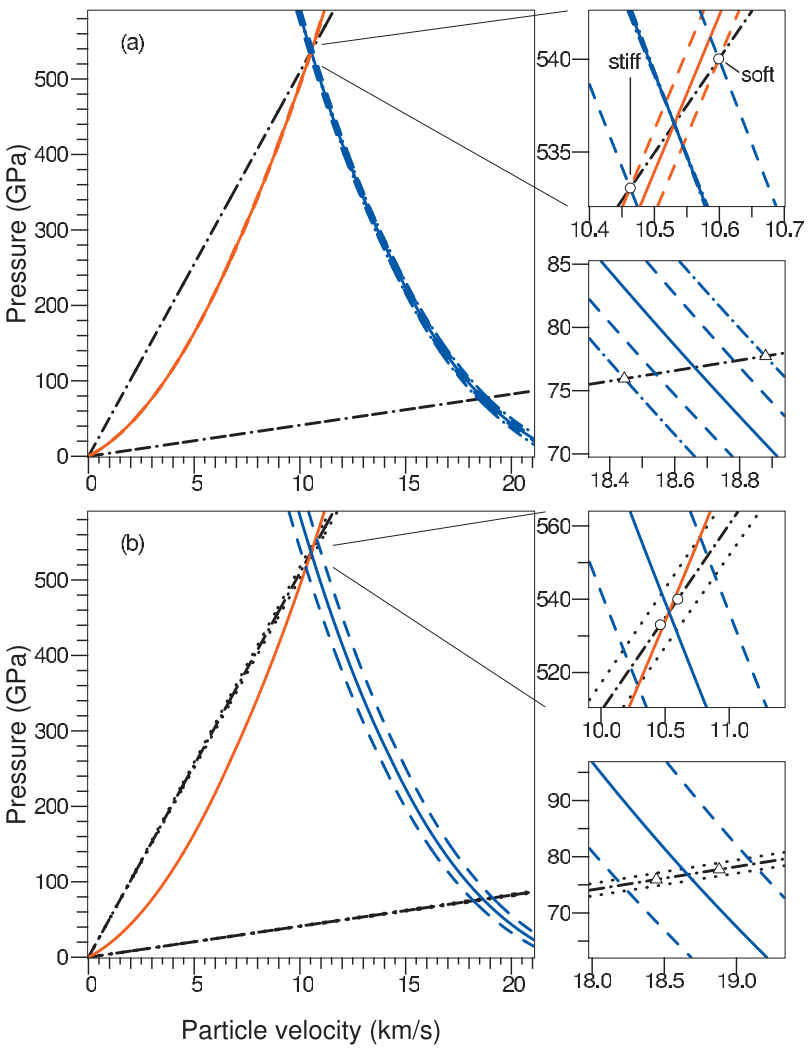

FIG. 4. (Color) Sample impedance-match diagram illustrating error propagation for a 537 GPa shock transmitted from Al into D_2. Black dashed-dotted curves show the Rayleigh lines. (a) Systematic uncertainties. Dashed curves show the systematic 1σ variations of the principal Hugoniot of Al relative to the best fit. Blue dashed-dotted curves show the addition of 1σ variations from the release profile, as estimated from the variations among an ensemble of five theoretical models as previously discussed (Ref. 56). (Insets) The open circles mark the range of systematic uncertainty in the Al Hugoniot state, while the open triangles mark the range of systematic uncertainty associated with the off-Hugoniot (release profile) uncertainty. (b) Random uncertainties. Black dotted curves show the range of uncertainty in the Rayleigh lines associated with the measurement uncertainties. Blue dashed curves show the propagation of uncertainty in the Al shock velocity, which is the dominant uncertainty. Scales in the insets are different; for comparison the open circles and open triangles from (a) are replotted in the insets in (b).

D_2 response is soft or stiff. Since these systematic errors can be comparable to the random uncertainties in our measurements, it is important that both are included in our analysis.

B. Initial density effects

The deuterium Hugoniot experiments carried out at the various facilities have been performed with different initial densities. These differences are much more significant when comparing experiments on initially solid (ρ_0=0.199 g/cm^3) (Refs. 28 and 29) or gaseous (ρ_0=0.153 and 0.134 g/cm^3) (Ref. 30) deuterium versus those on initially liquid deuterium: Nova (ρ_0=0.171 g/cm^3), Z (ρ_0=0.167 g/cm^3), and Omega (ρ_0=0.174 g/cm^3). Even though comparing the deuterium compression—rather than the absolute shock density—partially compensates for these different initial densities, residual differences can still be significant. Uncorrected comparison of these data results in small offsets between groups of data with different initial densities, both in the P-η and U_s-U_p planes.

To quantify such effects we investigate how the Hugoniot shifts with ρ_0 in two extreme D_2 EOS models, the stiff Sesame72 and soft Ross models, for initial densities in the range $0.11<\rho_0<0.23$ g/cm^3 and show how the same correction can be applied, irrespective of EOS model. Figures 5(a) and 5(d) compare the Hugoniots in the P-η plane and clearly illustrate how *higher* initial densities result in *lower* final compressions. This trend is seen in a wide variety of materials and is due primarily to the increasing interactions at higher densities. In the U_s-U_p plane, as shown in Figs. 5(b) and 5(e), these shifts result in a family of parallel lines separated in U_s by an amount that depends only on ρ_0. The change in U_s for a fixed U_p increases linearly with ρ_0 by an amount that is almost identical for both stiff and soft deuterium models. Thus, shifting a Hugoniot from one initial density (ρ_0) to another (ρ_{00}) requires simply adding a corrective term $\Delta C_0(\rho_0,\rho_{00})$ to U_s. By averaging over both models we find that $\Delta C_0(\rho_0,\rho_{00})[\mathrm{km/s}]=2.29(1-\rho_0/\rho_{00})$.

Figures 5(c) and 5(f) show how this corrective term successfully collapses Hugoniots from both stiff and soft models onto that from a single reference density which is, in this case, given by ρ_{00}=0.174 g/cm^3 (the value for our experiment). All the curves overlap to within $\pm$0.1 km/s over the range of interest for this study. This illustrates that our correction term $\Delta C_0(\rho_0,\rho_{00})$ while necessarily derived from deuterium EOS models, is largely independent of whether these models are stiff or soft.

TABLE I. Compilation of the deuterium impedance-match shock compression data from this work and from several previous studies, all analyzed using the same aluminum impedance-matching model described in the text. Results from this study are listed by shot number; results from Knudson *et al.* (Ref. 27) begin with a Z; data from Belov *et al.* (Ref. 28) and Boriskov *et al.* (Ref. 29) are listed as BKV-1 and BKV-2; data from Grishechkin *et al.* (Ref. 30) are listed as GRS-1 and GRS-2. Aluminum and deuterium initial densities are given by $\rho_{0\mathrm{Al}}$ and $\rho_{0\mathrm{D}}$; experimental observables were the D_2 shock speed ($U_{s\mathrm{D}}$) and either the Aluminum particle speed $U_{p\mathrm{D}}$ (for Z data only) or aluminum shock speed $U_{s\mathrm{Al}}$ (for all other data); the impedance-matched D_2 particle speed, pressure, and density are given by $U_{p\mathrm{D}}$, P_{D}, and ρ_{D}. The shift in $U_{s\mathrm{D}}$ to account for an initial density difference is given by ΔC_0; the resulting corrected shock speed, compression, and pressure are given by $U_{s\mathrm{D}_{\mathrm{corr}}}$, $\eta_{\mathrm{D}_{\mathrm{corr}}}$, and $P_{\mathrm{D}_{\mathrm{corr}}}$. For quantities with a systematic error component, random and systematic errors are listed in parentheses: (ran,sys).

Expt.	$\rho_{0\mathrm{Al}}$ (g cm^{-3})	$\rho_{0\mathrm{D}}$ (g cm^{-3})	$U_{s\mathrm{Al}}$ or $U_{p\mathrm{Al}}$ (km/s)	$U_{s\mathrm{D}}$ (km/s)	$U_{p\mathrm{D}}$ (km/s)	P_{D} (GPa)	ρ_{D} (mg cm^{-3})	ΔC_0 (km/s)	$U_{s\mathrm{D}_{\mathrm{corr}}}$ (km/s)	$\eta_{\mathrm{D}_{\mathrm{corr}}}$	$P_{\mathrm{D}_{\mathrm{corr}}}$ (GPa)
31700	2.740	0.174	26.07 ± 0.34	36.87 ± 0.33	28.96 ± (0.55,0.44)	186 ± (4,3)	811 ± (64,46)	0.00	36.87 ± 0.33	4.66 ± (0.37,0.26)	186 ± (4,3)
31692	2.740	0.174	21.88 ± 0.25	28.89 ± 0.32	23.04 ± (0.40,0.32)	116 ± (2,2)	859 ± (73,47)	0.00	28.89 ± 0.32	4.94 ± (0.42,0.27)	116 ± (2,2)
31912	2.740	0.174	18.75 ± 0.25	23.83 ± 0.32	18.50 ± (0.41,0.25)	77 ± (2,1)	778 ± (72,36)	0.00	23.83 ± 0.32	4.47 ± (0.42,0.21)	77 ± (2,1)
31910	2.740	0.174	15.51 ± 0.31	18.96 ± 0.31	13.77 ± (0.51,0.24)	45 ± (2,1)	635 ± (69,30)	0.00	18.96 ± 0.31	3.65 ± (0.40,0.17)	45 ± (2,1)
32248	2.740	0.174	23.30 ± 0.25	32.03 ± 0.32	25.00 ± (0.41,0.36)	139 ± (3,2)	793 ± (56,40)	0.00	32.03 ± 0.32	4.56 ± (0.32,0.23)	139 ± (3,2)
32252	2.740	0.174	25.65 ± 0.29	35.48 ± 0.39	28.43 ± (0.46,0.43)	176 ± (3,3)	876 ± (72,54)	0.00	35.48 ± 0.39	5.03 ± (0.42,0.31)	176 ± (3,3)
32254	2.740	0.174	27.08 ± 0.31	38.81 ± 0.31	30.38 ± (0.51,0.48)	205 ± (4,3)	802 ± (55,45)	0.00	38.81 ± 0.31	4.61 ± (0.32,0.26)	205 ± (4,3)
32258	2.740	0.174	27.96 ± 0.32	40.13 ± 0.31	31.66 ± (0.52,0.51)	221 ± (4,4)	824 ± (58,49)	0.00	40.13 ± 0.31	4.74 ± (0.33,0.28)	221 ± (4,4)
32864	2.740	0.174	19.45 ± 0.29	25.76 ± 0.34	19.44 ± (0.47,0.26)	87 ± (2,1)	709 ± (62,29)	0.00	25.76 ± 0.34	4.08 ± (0.36,0.17)	87 ± (2,1)
32866	2.740	0.174	21.67 ± 0.27	28.57 ± 0.39	22.73 ± (0.43,0.31)	113 ± (3,2)	852 ± (81,46)	0.00	28.57 ± 0.39	4.90 ± (0.47,0.26)	113 ± (3,2)
33190	2.740	0.174	25.89 ± 0.31	36.26 ± 0.34	28.74 ± (0.50,0.44)	181 ± (3,3)	839 ± (65,49)	0.00	36.26 ± 0.34	4.82 ± (0.38,0.28)	181 ± (3,3)
33194	2.740	0.174	23.24 ± 0.27	32.14 ± 0.34	24.90 ± (0.43,0.36)	139 ± (3,2)	772 ± (56,38)	0.00	32.14 ± 0.34	4.44 ± (0.32,0.22)	139 ± (3,2)
34135	2.740	0.174	20.55 ± 0.28	27.67 ± 0.34	21.02 ± (0.46,0.28)	101 ± (2,1)	724 ± (59,31)	0.00	27.67 ± 0.34	4.16 ± (0.34,0.18)	101 ± (2,1)
34139	2.740	0.174	23.58 ± 0.26	31.89 ± 0.31	25.47 ± (0.42,0.37)	141 ± (3,2)	864 ± (68,50)	0.00	31.89 ± 0.31	4.97 ± (0.39,0.29)	141 ± (3,2)
34144	2.740	0.174	22.51 ± 0.27	30.27 ± 0.37	23.91 ± (0.44,0.34)	126 ± (3,2)	829 ± (72,44)	0.00	30.27 ± 0.37	4.76 ± (0.41,0.25)	126 ± (3,2)
Z904N	2.740	0.167	5.27 ± 0.13	13.50 ± 0.24	9.69 ± (0.25,0.13)	22 ± (1,0)	592 ± (49,20)	0.09	13.59 ± 0.24	3.49 ± (0.29,0.12)	23 ± (1,0)
Z904S	2.740	0.167	5.27 ± 0.13	13.61 ± 0.27	9.70 ± (0.25,0.13)	22 ± (1,0)	581 ± (49,19)	0.09	13.70 ± 0.27	3.42 ± (0.29,0.11)	23 ± (1,0)
Z590	2.740	0.167	6.38 ± 0.29	15.26 ± 0.28	11.69 ± (0.55,0.14)	30 ± (1,0)	713 ± (120,29)	0.09	15.35 ± 0.28	4.19 ± (0.71,0.17)	31 ± (2,0)
Z895N	2.740	0.167	6.44 ± 0.16	15.41 ± 0.39	11.78 ± (0.32,0.15)	30 ± (1,0)	709 ± (89,29)	0.09	15.50 ± 0.39	4.17 ± (0.52,0.17)	32 ± (1,0)
Z895S	2.740	0.167	6.38 ± 0.16	15.72 ± 0.39	11.65 ± (0.31,0.14)	31 ± (1,0)	645 ± (70,23)	0.09	15.81 ± 0.39	3.80 ± (0.41,0.13)	32 ± (1,0)
Z698	2.740	0.167	6.38 ± 0.13	15.78 ± 0.15	11.64 ± (0.25,0.14)	31 ± (1,0)	636 ± (43,22)	0.09	15.87 ± 0.15	3.75 ± (0.25,0.13)	32 ± (1,0)
Z592	2.740	0.167	6.80 ± 0.31	15.99 ± 0.31	12.44 ± (0.60,0.16)	33 ± (2,0)	751 ± (139,34)	0.09	16.08 ± 0.31	4.41 ± (0.82,0.20)	35 ± (2,0)
Z792S	2.740	0.167	7.42 ± 0.15	17.91 ± 0.39	13.46 ± (0.29,0.19)	40 ± (1,1)	672 ± (66,28)	0.09	18.00 ± 0.39	3.96 ± (0.39,0.17)	42 ± (1,1)
Z824S	2.740	0.167	7.65 ± 0.16	17.97 ± 0.11	13.90 ± (0.31,0.20)	42 ± (1,1)	738 ± (59,36)	0.09	18.06 ± 0.11	4.34 ± (0.35,0.21)	44 ± (1,1)
Z792N	2.740	0.167	7.50 ± 0.15	17.98 ± 0.40	13.61 ± (0.29,0.19)	41 ± (1,1)	686 ± (70,30)	0.09	18.07 ± 0.40	4.05 ± (0.41,0.18)	43 ± (1,1)
Z824N	2.740	0.167	7.55 ± 0.16	18.02 ± 0.10	13.70 ± (0.31,0.19)	41 ± (1,1)	697 ± (52,31)	0.09	18.11 ± 0.10	4.11 ± (0.31,0.18)	43 ± (1,1)
Z1108	2.740	0.167	7.68 ± 0.18	18.34 ± 0.10	13.93 ± (0.35,0.20)	43 ± (1,1)	695 ± (57,31)	0.09	18.43 ± 0.10	4.10 ± (0.34,0.18)	45 ± (1,1)

TABLE I. (*Continued.*)

Expt.	$\rho_{0\mathrm{Al}}$ (g cm^{-3})	$\rho_{0\mathrm{D}}$ (g cm^{-3})	$U_{s\mathrm{Al}}$ or $U_{p\mathrm{Al}}$ (km/s)	$U_{s\mathrm{D}}$ (km/s)	$U_{p\mathrm{D}}$ (km/s)	P_{D} (GPa)	ρ_{D} (mg cm^{-3})	ΔC_0 (km/s)	$U_{s\mathrm{D}_{\mathrm{corr}}}$ (km/s)	$\eta_{\mathrm{D}_{\mathrm{corr}}}$	$P_{\mathrm{D}_{\mathrm{corr}}}$ (GPa)
Z593	2.740	0.167	7.84 ± 0.34	18.63 ± 0.15	$14.22 \pm (0.66, 0.21)$	$44 \pm (2, 1)$	$705 \pm (108, 33)$	0.09	18.72 ± 0.15	$4.16 \pm (0.64, 0.19)$	$46 \pm (2, 1)$
Z634	2.740	0.167	9.53 ± 0.20	22.48 ± 0.19	$17.03 \pm (0.37, 0.21)$	$64 \pm (1, 1)$	$689 \pm (51, 27)$	0.09	22.57 ± 0.19	$4.07 \pm (0.30, 0.16)$	$67 \pm (2, 1)$
Z711	2.740	0.167	9.98 ± 0.25	23.23 ± 0.19	$17.80 \pm (0.47, 0.21)$	$69 \pm (2, 1)$	$714 \pm (66, 27)$	0.09	23.32 ± 0.19	$4.22 \pm (0.39, 0.16)$	$72 \pm (2, 1)$
Z710	2.740	0.167	9.86 ± 0.20	23.25 ± 0.19	$17.57 \pm (0.37, 0.21)$	$68 \pm (2, 1)$	$683 \pm (49, 25)$	0.09	23.34 ± 0.19	$4.04 \pm (0.29, 0.15)$	$71 \pm (2, 1)$
Z1109S	2.740	0.167	9.99 ± 0.18	23.30 ± 0.36	$17.81 \pm (0.34, 0.21)$	$69 \pm (2, 1)$	$709 \pm (59, 27)$	0.09	23.39 ± 0.36	$4.19 \pm (0.35, 0.16)$	$72 \pm (2, 1)$
Z1109N	2.740	0.167	9.99 ± 0.18	23.43 ± 0.38	$17.80 \pm (0.34, 0.21)$	$70 \pm (2, 1)$	$695 \pm (58, 26)$	0.09	23.52 ± 0.38	$4.11 \pm (0.34, 0.15)$	$73 \pm (2, 1)$
Z712	2.740	0.167	9.88 ± 0.18	23.45 ± 0.22	$17.58 \pm (0.33, 0.21)$	$69 \pm (1, 1)$	$668 \pm (43, 24)$	0.09	23.54 ± 0.22	$3.95 \pm (0.25, 0.14)$	$72 \pm (1, 1)$
Z791S	2.740	0.167	9.88 ± 0.30	23.49 ± 0.41	$17.58 \pm (0.56, 0.21)$	$69 \pm (2, 1)$	$664 \pm (74, 23)$	0.09	23.58 ± 0.41	$3.93 \pm (0.44, 0.14)$	$72 \pm (3, 1)$
Z791N	2.740	0.167	9.88 ± 0.30	23.57 ± 0.50	$17.57 \pm (0.56, 0.21)$	$69 \pm (3, 1)$	$656 \pm (77, 23)$	0.09	23.66 ± 0.50	$3.89 \pm (0.46, 0.13)$	$72 \pm (3, 1)$
Z894	2.740	0.167	10.35 ± 0.16	24.10 ± 0.22	$18.42 \pm (0.30, 0.21)$	$74 \pm (1, 1)$	$709 \pm (45, 27)$	0.09	24.19 ± 0.22	$4.19 \pm (0.26, 0.16)$	$78 \pm (1, 1)$
Z893	2.740	0.167	10.38 ± 0.16	24.56 ± 0.27	$18.43 \pm (0.30, 0.21)$	$76 \pm (1, 1)$	$669 \pm (41, 23)$	0.09	24.65 ± 0.27	$3.96 \pm (0.25, 0.14)$	$79 \pm (2, 1)$
Z1111N	2.740	0.167	10.80 ± 0.17	24.94 ± 0.44	$19.18 \pm (0.32, 0.22)$	$80 \pm (2, 1)$	$723 \pm (62, 28)$	0.09	25.03 ± 0.44	$4.28 \pm (0.37, 0.17)$	$84 \pm (2, 1)$
Z1111S	2.740	0.167	10.80 ± 0.17	25.30 ± 0.46	$19.15 \pm (0.32, 0.22)$	$81 \pm (2, 1)$	$687 \pm (56, 25)$	0.09	25.39 ± 0.46	$4.07 \pm (0.33, 0.15)$	$85 \pm (2, 1)$
Z1110N	2.740	0.167	11.37 ± 0.17	26.11 ± 0.47	$20.14 \pm (0.32, 0.24)$	$88 \pm (2, 1)$	$730 \pm (63, 29)$	0.09	26.20 ± 0.47	$4.32 \pm (0.37, 0.17)$	$92 \pm (2, 1)$
Z1110S	2.740	0.167	11.37 ± 0.17	26.44 ± 0.50	$20.10 \pm (0.32, 0.23)$	$89 \pm (2, 1)$	$697 \pm (59, 26)$	0.09	26.53 ± 0.50	$4.13 \pm (0.35, 0.15)$	$93 \pm (2, 1)$
Z946	2.740	0.167	12.12 ± 0.49	28.00 ± 0.57	$21.38 \pm (0.93, 0.25)$	$100 \pm (5, 1)$	$706 \pm (112, 27)$	0.09	28.09 ± 0.57	$4.18 \pm (0.66, 0.16)$	$104 \pm (5, 1)$
BKV-1	2.740	0.199	16.39 ± 0.10	20.30 ± 0.20	$14.81 \pm (0.16, 0.23)$	$60 \pm (1, 1)$	$736 \pm (31, 32)$	−0.33	19.97 ± 0.20	$3.87 \pm (0.16, 0.17)$	$51 \pm (1, 1)$
BKV-2	2.740	0.199	21.20 ± 0.30	28.20 ± 0.60	$21.62 \pm (0.48, 0.29)$	$121 \pm (3, 2)$	$853 \pm (92, 37)$	−0.33	27.87 ± 0.60	$4.46 \pm (0.48, 0.20)$	$105 \pm (3, 1)$
GRS-1	2.700	0.153	20.40 ± 0.30	27.95 ± 0.60	$21.15 \pm (0.49, 0.29)$	$90 \pm (3, 1)$	$628 \pm (65, 27)$	0.28	28.23 ± 0.60	$3.99 \pm (0.41, 0.17)$	$104 \pm (3, 1)$
GRS-2	2.700	0.134	20.40 ± 0.30	28.02 ± 0.40	$21.49 \pm (0.49, 0.30)$	$80 \pm (2, 1)$	$573 \pm (53, 26)$	0.53	28.55 ± 0.40	$4.04 \pm (0.37, 0.19)$	$107 \pm (3, 1)$

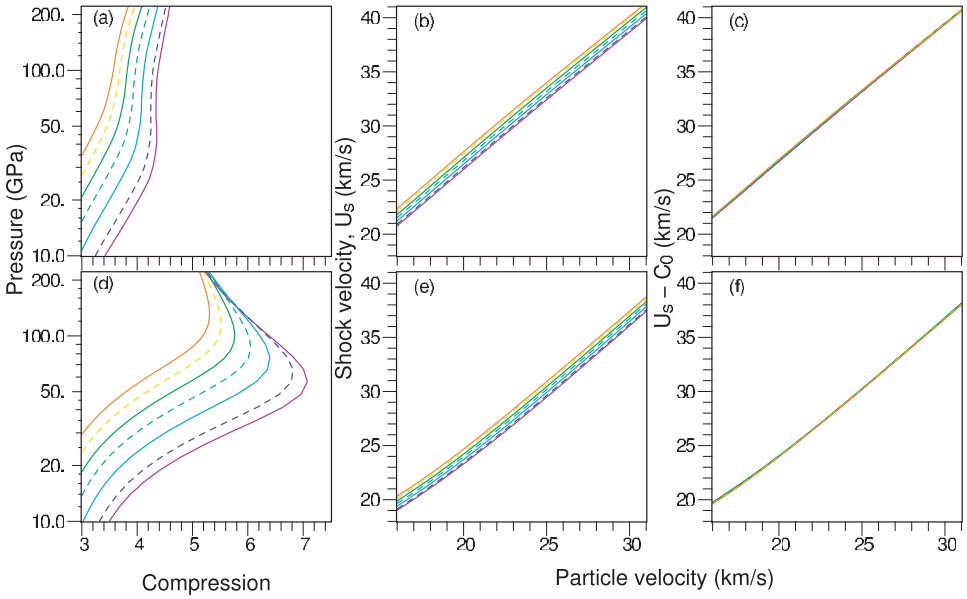

FIG. 5. (Color) Comparison of (a)–(c) Sesame72 (Ref. 8) and (d)–(f) Ross (Ref. 10) deuterium Hugoniot predictions for a suite of initial densities: 0.1, 0.12, 0.14, 0.16, 0.18, 0.20, and 0.22 g/cm^3 shown alternately as solid and dashed curves; colors range from violet (less dense) to red (more dense). (a) and (d) show pressure versus compression and illustrate how lower initial densities produce higher peak compressions; (b) and (e) show U_s versus U_p and illustrate how the different initial densities produce slightly offset yet parallel Hugoniots; (c) and (f) show how by adding an offset correction (ΔC_0) to U_s causes these parallel Hugoniots to collapse onto a common curve. This correction is the same for both stiff (Sesame72) and soft (Ross) models and provides a way to directly compare experiments performed at different initial densities.

V. RESULTS

A. Shock velocity observables

It is instructive to compare results for the shock observables $U_{s\mathrm{D}}$ and $U_{s\mathrm{Al}}$ since these are typically the inputs to the impedance-matching calculations. Figure 6 shows our $U_{s\mathrm{D}}$ vs $U_{s\mathrm{Al}}$ data (also listed in Table I) along with the data of Knudson *et al.*,[26,27] Boriskov *et al.*,[29] Grishechkin *et al.*,[30] and Belov *et al.*[28] It should be noted that, in the case of the Knudson *et al.* experiments only, $U_{s\mathrm{Al}}$ was not an observable. They measured the flyer velocity $\sim 2U_{p\mathrm{Al}}$ to infer the shock state in Al. For these data we reconstructed the $U_{s\mathrm{Al}}$ from our best fit Hugoniot and some additional information given in Knudson *et al.*[68] As discussed previously,[27,56] the use of $U_{p\mathrm{Al}}$ rather than $U_{s\mathrm{Al}}$ as an observable changes slightly the way systematic errors in the Al EOS are propagated, considerably reducing the effect of uncertainties in the principal Hugoniot. Errors in the release are unchanged. In practice, the errors in those experiments below 100 GPa are largely dominated by the random uncertainties.

The results in Fig. 6 show that the single shock Al-D_2 experiments in the impedance-match configuration produce universal agreement in the experimental observables *regardless of driver*, at least in the pressure range where multiple data sets exist. Two theoretical curves are shown for reference: the Sesame72 (Ref. 8) and the Ross model;[10] these curves were calculated using the Al impedance-matching model described above, assuming an initial deuterium density of 0.174 g/cm^3. Note how, above the highest pressure points obtained in the Z experiments (28 km/s or 100 GPa), the data reported here appear to shift from near agreement with the stiffer model partially toward the softer deuterium model. This softening trend is also indicated by a single convergent-explosive data point[29] around 28 km/s.

B. Principal Hugoniot

The principal Hugoniot data for this experiment are shown in Figs. 7 and 8 and include both random and systematic uncertainties. These data are shown along with those from Knudson *et al.*,[27] Belov *et al.*,[28] Boriskov *et al.*,[29,31] and Grishechkin *et al.*[30]

In order to determine whether the use of different Al EOS models by previous workers could cause systematic shifts between each data set, where possible we reanalyzed previous data according to the procedure described in Sec. IV A. The results, along with our data, are shown in Table I and include both systematic and random error components where applicable. The Al EOS model originally used by Grishechkin *et al.*[30] appears to have been significantly softer than the model used here since these data become stiffer when reanalyzed with our best fit Al model. The Al model used by Belov *et al.*[28] was also softer whereas that used by Boriskov *et al.*[29] was very slightly stiffer than ours at the relevant pressures. Other experiments by Boriskov *et al.*[31] did not report aluminum shock velocities and thus could not be reanalyzed. As discussed in Sec. IV A, Knudson *et al.* used an Al EOS that was too stiff at the highest pressures; their data become slightly softer when analyzed using our Al model. The stiffness of our best-fit Al model thus appears to be somewhere in between those used previously.

All data have been normalized to the initial liquid density of $\rho_{00}=0.174$ g/cm^3 used in this experiment by applying the

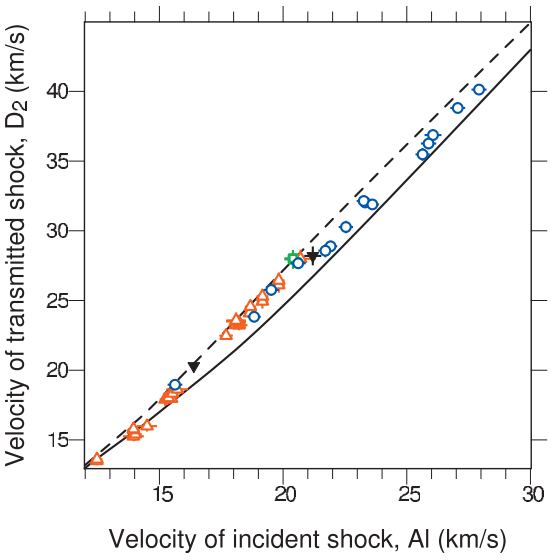

FIG. 6. (Color) Raw data for D_2 impedance-match experiments with Al as the standard. Data are from Knudson *et al.* (Ref. 27). (open red triangles), Belov *et al.* (Ref. 28), Boriskov *et al.* (Ref. 29) (inverted black solid triangles), Grishechkin *et al.* (Ref. 30) (open green squares, with two points overlapped on this plot), and this work (open blue circles). The solid (dashed) curve is a prediction from the Ross (Sesame72) model when impedance matched to our best fit Al impedance-match model. This plot provides the closest comparison of raw experimental observables among all the impedance-match experiments.

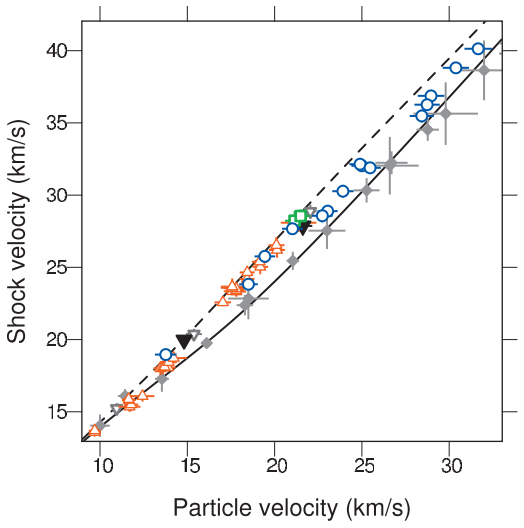

FIG. 7. (Color) U_s versus U_p data for the deuterium principal Hugoniot. Impedance-match results from Knudson *et al.* (Refs. 26 and 27) (red triangles), Belov *et al.* (Ref. 28), Boriskov *et al.* (Ref. 29) (inverted black solid triangles), Boriskov *et al.* (Ref. 31) (inverted black open triangles), Grishechkin *et al.* (Ref. 30) (open green squares), and this work (solid blue circles). Absolute Hugoniot measurements are from Da Silva *et al.* (Ref. 23) and Collins *et al.* (Refs. 24 and 25) (gray diamonds). Solid (dashed) curve shows the Hugoniot predicted by the Ross (Ref. 10) (Sesame72 (Ref. 8)) model. Error bars for the impedance-match data represent the quadrature sum of the random and systematic errors in the impedance-match analysis.

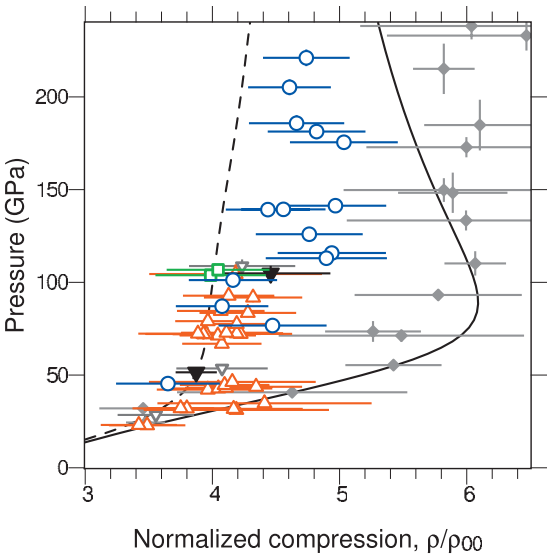

FIG. 8. (Color) Pressure versus compression for single shock measurements of the deuterium Hugoniot. Impedance-match results from Knudson *et al.* (Refs. 26 and 27) (red triangles), Belov *et al.* (Ref. 28), Boriskov *et al.* (Ref. 29) (inverted black solid triangles), Boriskov *et al.* (Ref. 31) (inverted black open triangles), Grishechkin *et al.* (Ref. 30) (open green squares), and this work (open blue circles). Absolute Hugoniot measurements are from Da Silva *et al.* (Ref. 23) and Collins *et al.* (Refs. 24 and 25) (gray diamonds). Solid (dashed) curve shows the Hugoniot predicted by the Ross (Ref. 10) (Sesame72 (Ref. 8)) model. For proper comparison, impedance-match data from all experiments have been (i) analyzed using the same Al model (as described in this paper) and (ii) normalized to the initial density of $\rho_{00}=0.174$ g/cm^3 used in this experiment.

method described in Sec. IV B. These adjustments result in very small corrections to data from other experiments using liquid samples. For example, the data from Z, taken at $\rho_0=0.167$ g/cm^3 becomes stiffer by around 1% in compressibility. However, the data from nonliquid samples, which have considerably larger differences in initial density, undergo around 5% changes in compressibility. Data from solid deuterium samples[28,29] ($\rho_0=0.199$ g/cm^3) become softer[41] while data from gas samples[30] ($\rho_0=0.153$ and 0.134 g/cm^3) appear stiffer. Note that, by necessity, pressures are also changed slightly by this correction. The values of the required ΔC_0 corrections for each experimental point are listed in Table I along with the final adjusted pressure ($P_{\mathrm{D}_{\mathrm{corr}}}$) and compression ($\eta_{\mathrm{D}_{\mathrm{corr}}}$).

Below 110 GPa, the data reported here are consistent with all previously reported IM results which show a stiff response for deuterium. The inferred 4.0–4.5-fold deuterium compression disagrees with four data points from the Nova absolute data in the range $50<P_{\mathrm{Al}}<100$ GPa which show a softer response. Above 110 GPa the centroid of our data exhibits a softening up to fivefold compression, remaining between 4.5 and fivefold compressions up to above 200 GPa. This is systematically stiffer than the sixfold compression observed in the Nova radiography experiments. After correcting for initial density effects, several convergent-explosive points cluster between 100 and 110 GPa, with one point[29] suggesting a softening to $\eta=4.5$. No published

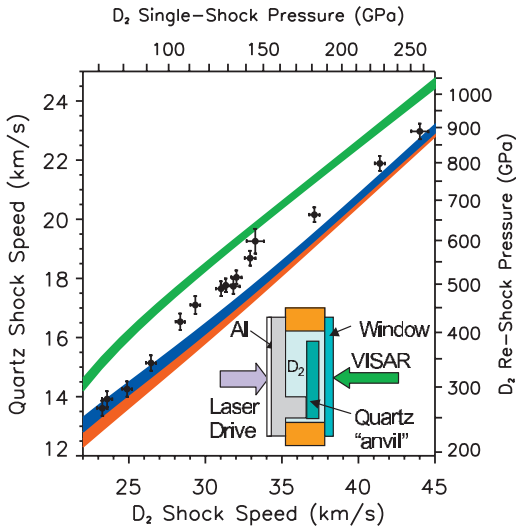

FIG. 9. (Color) Experimental observables for the double shock experiments of Boehly *et al.* (Ref. 32) together with model calculations from Ross (Ref. 10) (green line), Sesame72 (Ref. 8) (red line), and Kerley03 (Ref. 34) (blue line). The data are consistent with stiff models below ~100 GPa but lie in between stiff and soft models at higher pressures. The width of the model EOS lines gives the uncertainty in the quartz Hugoniot. Inset shows the target arrangement for the double shock experiment (Ref. 75).

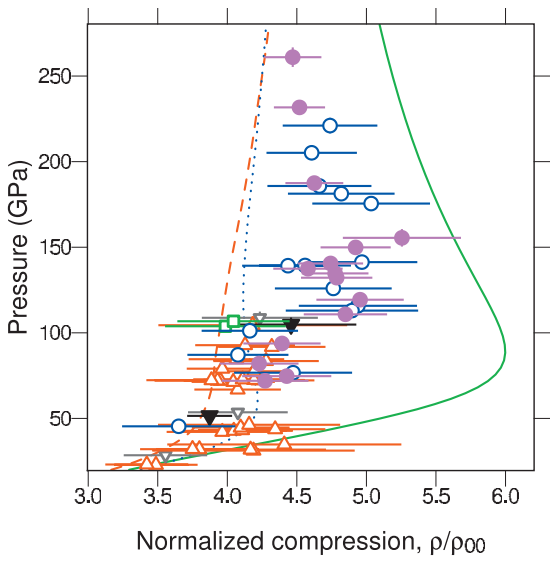

FIG. 10. (Color) Single shock Hugoniot inferred from double shock data of Boehly *et al.* (Ref. 32) using the inversion method described in Appendix A (solid pink circles). Also shown are the single shock impedance-match measurements of this study (open blue circles), Knudson *et al.* (Refs. 26 and 27) (red triangles), Belov *et al.* (Ref. 28), Boriskov *et al.* (Ref. 29) (inverted black solid triangles), Boriskov *et al.* (Ref. 31) (inverted black open triangles), and Grishechkin *et al.* (Ref. 30) (open green squares). The agreement between the laser-driven single and double shock results over all pressures indicates that the systematics for each type of measurement, which differ significantly, have been estimated correctly. Both sets of data exhibit an abrupt increase in compression around 110 GPa. Model curves are from Sesame72 (dashed red), Kerley03 (dotted blue), and Ross EOS (solid green).

magnetic-flyer data exist above 104 GPa. It is unfortunate that all previously published explosive-driven and magnetic-flyer-driven measurements fall just short of the pressures where we observe an additional softening of the Hugoniot.

Comparing to *ab initio* calculations above 110 GPa, these results are softer than those given by the restricted PIMC approach of Militzer *et al.*[20] but in agreement with the direct PIMC calculation of Filinov *et al.*[22] which shows fivefold compression above 100 GPa. DFT calculations by Desjarlais[17] do not show any softening at such high pressure, predicting instead that $\eta < 4.3$ above 100 GPa; other DFT calculations have not been reported up to these pressures.

VI. COMPARISONS WITH PREVIOUS LASER-DRIVEN MULTIPLE SHOCK MEASUREMENTS

A. Double shock pressures

Double shock measurements are a useful way to assess the deuterium single shock compression since the second-shock pressure is very sensitive to the first-shock density. Laser double shock experiments at Omega were performed previously[32] using a highly precise quartz anvil technique. The laser conditions and diagnostics were identical to those described above. A diagram of the target arrangement is shown in the inset of Fig. 9, illustrating the quartz reshock anvil positioned 35 μm into the deuterium. The experimental observables were the deuterium single shock velocity and the quartz shock velocity and are shown in Fig. 9. When compared to reshock predictions from various EOS models, these experiments showed that deuterium has a stiff response below first-shock pressures of ~100 GPa and a softer response above. The similarity of this behavior with the single shock data shown in Fig. 8 is evident.

To more quantitatively compare these previous double shock measurements with the present laser-driven single shock data, a method to transform the double shock observables (shown in Fig. 9) into the single shock P-η plane has been developed. This was done by converting the measured second-shock pressure and first-shock velocity into a single shock density and pressure via the Hugoniot relations using an average of several models to determine the second-shock compressibility of deuterium. Details of this method are given in Appendix A. This approach is predicated on the idea that the second-shock compressibility is much less uncertain than the first shock compressibility. The variations observed in several EOS models show that this assumption appears to be reasonable. Although the models predict severe differences in first-shock compressibilities, they all give very similar second-shock compressibilities (see Fig. 14). Using a model-based estimate of the second-shock compressibility to interpret the reshock data thus appears to be a complementary way of estimating the first-shock compressibility.

The principal Hugoniot derived in this way from the double shock data of Boehly *et al.*[32] is given by the filled circles in Fig. 10 and listed in Table II. Error bars represent a quadrature sum of both the random and systematic uncertainties. Systematic errors in this inversion technique arise from

TABLE II. Single shock properties as inferred from the inversion of double shock data reported by Boehly *et al.* (Ref. 32) using the technique described in Appendix A and the model-averaged $\tilde{\gamma}$ shown in Fig. 13. U_{sD1} and U_{sQ} are the measured shock speeds in D_2 and quartz; U_{pD1}, P_{D1}, ρ_{D1}, and η_D are the inferred single shock particle speed, pressure, density, and compression in deuterium. For quantities with a systematic error component the random and systematic errors are listed separately in parentheses: (ran,sys).

Expt.	U_{sD1} (km/s)	U_{sQ} (km/s)	U_{pD1} (km/s)	P_{D1} (GPa)	ρ_{D1} (mg cm^{-3})	η_D
27869	37.12 ± 0.34	20.15 ± 0.25	29.09 ± (0.29,0.13)	187.5 ± (2.9,0.8)	803 ± (32,13)	4.63 ± (0.19,0.07)
27879	29.35 ± 0.32	17.10 ± 0.30	23.43 ± (0.32,0.13)	119.4 ± (2.4,0.7)	860 ± (50,19)	4.95 ± (0.29,0.11)
27934	32.92 ± 0.35	18.68 ± 0.25	26.23 ± (0.28,0.13)	149.9 ± (2.7,0.7)	855 ± (39,16)	4.92 ± (0.23,0.09)
27940	31.83 ± 0.41	17.73 ± 0.25	24.88 ± (0.30,0.14)	137.5 ± (2.9,0.8)	795 ± (39,16)	4.58 ± (0.22,0.09)
29012	16.68 ± 0.47	9.21 ± 0.63	11.20 ± (0.96,0.41)	32.4 ± (2.9,1.2)	528 ± (100,37)	3.04 ± (0.58,0.21)
29021	24.88 ± 0.32	14.26 ± 0.26	19.00 ± (0.31,0.18)	82.0 ± (1.9,0.8)	734 ± (42,22)	4.23 ± (0.24,0.13)
29398	44.01 ± 0.56	22.97 ± 0.26	34.16 ± (0.33,0.15)	261.0 ± (5.0,1.1)	776 ± (33,11)	4.47 ± (0.19,0.07)
29401	41.40 ± 0.33	21.89 ± 0.25	32.24 ± (0.29,0.14)	231.7 ± (3.2,1.0)	784 ± (28,12)	4.52 ± (0.16,0.07)
29412	23.27 ± 0.33	13.61 ± 0.26	17.82 ± (0.30,0.19)	72.0 ± (1.8,0.8)	742 ± (46,25)	4.27 ± (0.27,0.15)
30122	28.36 ± 0.30	16.53 ± 0.28	22.51 ± (0.30,0.14)	110.8 ± (2.2,0.7)	842 ± (47,20)	4.85 ± (0.27,0.11)
30129	33.26 ± 0.56	19.26 ± 0.42	26.93 ± (0.45,0.12)	155.5 ± (4.4,0.7)	912 ± (70,17)	5.26 ± (0.41,0.10)
30134	31.33 ± 0.33	17.77 ± 0.23	24.77 ± (0.26,0.13)	134.7 ± (2.4,0.7)	829 ± (37,17)	4.78 ± (0.21,0.10)
30663	32.03 ± 0.34	18.04 ± 0.23	25.28 ± (0.26,0.13)	140.5 ± (2.5,0.7)	823 ± (36,16)	4.74 ± (0.21,0.09)
31359	31.03 ± 0.34	17.65 ± 0.25	24.55 ± (0.28,0.13)	132.2 ± (2.4,0.7)	831 ± (40,17)	4.79 ± (0.23,0.10)
31361	26.45 ± 0.32	15.14 ± 0.26	20.43 ± (0.30,0.17)	93.8 ± (2.0,0.8)	763 ± (42,21)	4.39 ± (0.24,0.12)
31363	23.58 ± 0.34	13.92 ± 0.26	18.25 ± (0.30,0.18)	74.7 ± (1.9,0.7)	769 ± (48,26)	4.43 ± (0.28,0.15)

uncertainties in the second-shock compressibility, which we define to be the variations in the model-based predictions of the adiabatic exponent (see Fig. 13) combined with uncertainties in the measured quartz Hugoniot.[53] The quadrature sum of these systematic errors is found to be $<4\%$ in the first-shock density for pressures higher than 100 GPa. Comparison of the results in Fig. 10 with the impedance-match data (open circles) shows that the double shock data of Boehly *et al.*[32] are consistent with the single shock data presented in Figs. 7 and 8.

The common conclusion from both data sets is that the single shock density compression of liquid deuterium reaches a peak of $\eta=5.0$, intermediate between the stiffest and softest models, at pressures between ~110 and ~200 GPa. The agreement between single shock and inverted double shock results is of particular significance because the systematics of the two analyses are fundamentally different. In the impedance-match analysis the model-dependent uncertainty of the aluminum release and data-dependent uncertainty of the aluminum Hugoniot determine the total systematic uncertainty; in the inverted double shock analysis the model-dependent estimate of the deuterium second-shock compressibility and the data-dependent uncertainty of the quartz Hugoniot determine the systematic uncertainty. However, for both cases our estimates indicate that the total *systematic* uncertainties in compression are similar, about $\delta\eta_{sys}/\eta<4\%$, which is smaller than the measurement uncertainties in all cases. The comparison in Fig. 10 shows that the Hugoniots estimated from single shock impedance-match data and from double shock data are statistically identical, providing confidence that the systematics for both measurements has been accounted for correctly.

Combining the single and double shock data it is apparent that the softening of deuterium around 110 GPa is quite abrupt, suggestive of a ~15% density discontinuity. It is reasonable to question whether this abrupt softening, observed under both single and double shock compressions, is merely an artifact of the high-pressure behavior of quartz since quartz is used in both the single shock measurements (as a velocity gauge) and the double shock measurements (as a reshock anvil). However, this cannot be the case since a pressure of 110 GPa in deuterium corresponds to different pressures in quartz depending on the experimental arrangement: 7.5 Mbar (21.5 km/s) in the single shock arrangement [Fig. 2(a)] and 4 Mbar (16.5 km/s) in the double shock arrangement (see inset of Fig. 9). Furthermore, no corresponding anomalies were observed in quartz Hugoniot measurements taken on different experimental platforms (see Ref. 53 and references therein).

B. Shock wave reverberation times

Shock wave reverberation times were shown in the magnetic-flyer plate experiments[27,44] to be sensitive to the single shock density. Since the laser-driven reshock experiments of Boehly *et al.*[32] also generated multiple reverberations in the compressed deuterium (see Fig. 2 of that reference), a similar type of analysis is attempted here. However, unlike the single and double shock measurements described above, which were performed essentially at an instant, these reverberation data are necessarily time-integrated measurements and therefore extremely sensitive to unsteadiness in the shock wave velocities. Given that shock velocities in our experiments vary by a few percent during transit, hydrody-

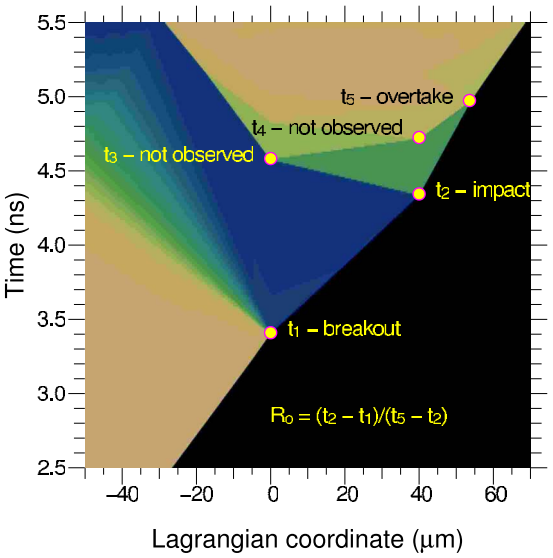

FIG. 11. (Color online) Space-time diagram of deuterium shock reverberation occurring between an Al pusher and quartz anvil. Only the leading shock front is observed in these experiments and not the interface as was done in a previous study (Ref. 44); this is because pressures are sufficiently high in both deuterium and quartz that the shocks are reflecting to the VISAR diagnostic. Hence only events 1, 2, and 5 are recorded.

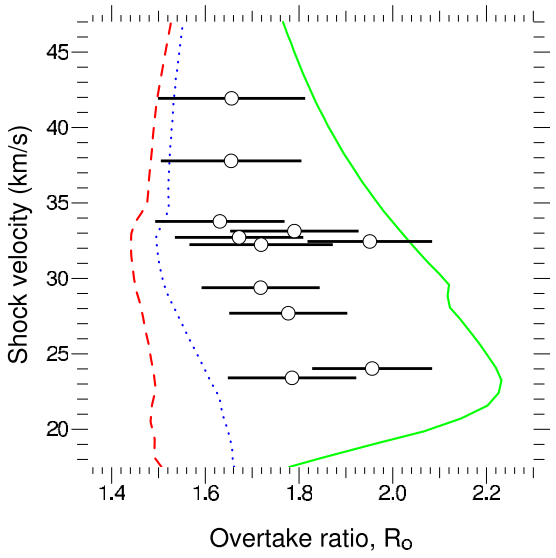

FIG. 12. (Color online) The overtake ratio R_O plotted versus average deuterium shock speed. Model curves are from Sesame72 (dashed red), Kerley03 (dotted blue), and Ross EOS (solid green). Unlike the single and double shock measurements described in this study, these reverberation time data are extremely sensitive to unsteady shock wave profiles. Approximate corrections for this have been applied using the method described in Appendix B.

namic simulations were required to provide corrections for shock unsteadiness. At the highest pressures accessed in our experiments these corrections spanned more than half the difference between stiff and soft behaviors. Nevertheless, we report our best attempt to quantitatively analyze this type of measurement since it was integral to the case built by Knudson *et al.*[44] for the compressibility of deuterium below 75 GPa.

The experimental setup was the same as that for the reshock measurements and is shown in the inset to Fig. 9. Details of the shock wave reverberations between the aluminum pusher and the quartz anvil are shown in the space-time diagram in Fig. 11. Although there are several reverberation events, only three of these are directly observable: t_1 is the time that the shock is initially transmitted into the D_2 sample from the Al pusher, t_2 is the time that the shock impacts the quartz anvil, and t_5 is the time that the reverberation overtakes the initial shock in the quartz anvil. The last event occurs after the shock wave has made three transits through the D_2 sample. We define $R_O=(t_2-t_1)/(t_5-t_2)$ to be the overtake ratio, analogous to the overtake ratio defined by Knudson *et al.*[44] The difference between this technique and the one used by Knudson *et al.* is that our earliest observation of the reverberation is at the catch-up time t_5, while Knudson *et al.* monitored the reverberation signature at the deuterium-anvil interface, or event t_4 as represented in Fig. 11. This is because, at the pressures reported in Boehly *et al.*,[32] the shocked quartz becomes optically reflecting,[52] blocking the deuterium-quartz interface from view.

The relationship between the inferred single shock compression and the observed R_O is very sensitive to the steadiness of the wave and the flow conditions well behind the shock front and requires hydrodynamic simulations for proper interpretation. To avoid introducing additional uncertainty from the inherent errors in any single hydrodynamic simulation an ensemble of simulations was performed to derive a scaling relation between the change in shock velocity δU_{sD} and the resulting change in overtake ratio δR_O for a *monotonically* decaying (or accelerating) shock velocity. As described in Appendix B, decaying shock waves tend to give artificially low values of R_O (making the data appear excessively stiff) and therefore must be corrected *upward*.

Figure 12 shows the corrected R_O as a function of U_{sD}. The calculated error bars are dominated by the ~40 ps random measurement error in determining each of the times t_1, t_2, and t_5 from each data record. A major problem with this type of measurement is that systematic errors are difficult to quantify and almost impossible to propagate in the analysis; the errors shown are thus most likely an *underestimate* of the true uncertainty in the measurement. In particular, the shock steadiness correction assumes a monotonically decaying shock wave profile. While the subset of reshock data we used in this reverberation analysis appeared to exhibit this type of general behavior, the wave profile behind the shock front is impossible to know and can have a significant impact on the reverberation time. In addition, several EOS uncertainties such as the EOS of Al under a compression-release-recompression cycle and quartz under double compression are not known. Despite these caveats, the curves displayed in Fig. 12 are generally consistent with the impedance-match analysis and the double shock results, i.e., a shock compression that lies intermediate between the stiff and soft models.

VII. DISCUSSION AND CONCLUSIONS

A set of laser-driven shock experiments indicate that the deuterium Hugoniot is stiff ($\eta \simeq 4.2$) between 50 and 100

GPa, becoming softer ($\eta \simeq 5.0$) above 110 GPa. Very similar behavior was also observed previously in laser-driven double shock measurements.[32] The consistency between these two types of measurement, each with distinctly different systematics, provides good confidence in the results. These data are in agreement with those from magnetically driven flyers[27] and convergent explosives,[28,29] although those previous results were restricted to pressures below 110 GPa, where we find the Hugoniot to be stiff. Around 105 GPa, a trend toward a softer Hugoniot is suggested perhaps by a single convergent-explosive point;[29] however, this will need to be confirmed in magnetic-flyer and explosive experiments above 110 GPa.

These laser-shock data, taken using impedance-matching techniques, disagree with the 5.5-fold to sixfold compressions observed in the first laser-shock experiments[23,24] which had implemented a radiography technique. It thus appears that the differences between the early laser-shock measurements and subsequent deuterium Hugoniot measurements performed on other platforms are not due to the different time scales of each shock experiment and are likely a result of limitations in the radiography measurement technique. Other workers[69] have suggested that shock tilt, steadiness, and preheat effects caused systematic errors in the Nova experiments; however, those issues were identified and addressed in the initial experiments, as well as in subsequent reanalysis, and cannot quantitatively explain the results. Ultimately the radiography measurements need to be carefully repeated to identify where the discrepancy arises.

Considerable attention has been given in this experiment to establishing the pedigree of the aluminum impedance-matching model and to propagating uncertainties in the aluminum Hugoniot and release curves. We have developed an impedance-match technique with minimal model dependence[56] based on the best fit to absolute Al Hugoniot data and applied it both to our data as well as to previous results, propagating errors throughout. This best-fit Al model approach does not significantly affect previously published results below 100 GPa but is very important for analyzing data much above 100 GPa. In addition to standardizing the aluminum impedance-matching analysis, we have corrected for the effects of different initial densities used in the various experiments. This is particularly important when trying to compare the convergent-explosive measurements performed on nonliquid samples.[41]

Above 110 GPa, the resulting Hugoniot we observe is in agreement with direct PIMC (Refs. 21 and 22) calculations which show fivefold compression but are in disagreement with restricted PIMC calculations by Militzer and Ceperley[20] and the DFT results of Desjarlais[17] both of which predict that deuterium remains below 4.2-fold compressed at these pressures. DFT predictions by other workers do not extend above 100 GPa.

The ~15% increase in compression around 110 GPa may be suggestive of a phase transition in the fluid, the existence of which has been predicted in some first-principles calculations.[19,70–72] Recent experiments on deuterium under quasi-isentropic compression observed a 20% density discontinuity around 1.4 g/cm^3 and 130 GPa, appearing to confirm the existence of a first-order transition at low temperatures.[73] Scandolo *et al.*[71] suggested that at higher temperatures the critical point of a liquid-liquid phase boundary could cause increased compressibility[74] along the nearby Hugoniot. These scenarios would need to be consistent with both single and double shock measurements. Better evidence for a phase transition or critical point will likely come from measurements of thermodynamic derivatives such as the sound speed or specific-heat capacity.[52]

ACKNOWLEDGMENTS

We thank the Omega operations crew for the help in carrying out the experiments, Mark Bonino and the Omega target fabrication group for their outstanding work, G. Kerley for providing his EOS tables, and Walter Unites for his assistance throughout. This work was performed under the auspices of the U.S. Department of Energy by Lawrence Livermore National Laboratory in part under Contract No. W-7405-Eng-48 and in part under Contract No. DE-AC52-07NA27344 and by the University of Rochester under Cooperative Agreement No. DE-FC03-92SF19460.

APPENDIX A: INFERRING SINGLE SHOCK COMPRESSION FROM DOUBLE SHOCK MEASUREMENTS

We have developed a method to infer the single shock compression from the velocities measured in a deuterium double shock experiment. This technique requires solving the Hugoniot equations using input from EOS models to determine the second-shock compressibility. Uncertainties in the second-shock compressibility, based on an average of stiff and soft models, are propagated in the analysis.

Before describing this technique, it is important to understand the observables measured in the reflected shock experiment.[32] Here an incident shock at velocity U_{sD} in deuterium traverses a reservoir of liquid D_2 and impacts a quartz anvil, launching a reflected shock (reshock) in deuterium and a transmitted shock at velocity U_{sQ} in the quartz anvil (see inset to Fig. 9). Since both deuterium and quartz are transparent, U_{sD} is measured immediately before impact while U_{sQ} is measured immediately after impact, as required for impedance-match calculations at an interface. Because the doubly shocked deuterium and singly shocked quartz equilibrate to a common pressure at the interface and because the quartz Hugoniot is known to high accuracy, by measuring U_{sQ} we know the reshock pressure in deuterium to high accuracy. Figure 9 shows the (model-independent) experimental observables for the reshock experiment together with reshock observables calculated using the Ross and Sesame72 models. Without any further analysis, the similarity between the single shock IM data in Figs. 7 and 8 and the laser reshock data is apparent by the way the data lie nearer the stiff Sesame72 predictions at lower pressures and approximately midway between the Ross and Sesame72 models at higher pressures.

The method by which the first-shock density can be deduced from the reshock observables becomes apparent from examining the set of Hugoniot equations for single and

double shocks. Using a single model-dependent dimensionless parameter for the second-shock (in)compressibility results in five equations and five unknowns, fully determining the system of equations. The Hugoniot equations for a single shock in deuterium are given by

$$\rho_{D1}(U_{sD1} - U_{pD1}) = \rho_{D0}U_{sD1}, \tag{A1}$$

$$P_{D1} = \rho_{D0}U_{sD1}U_{pD1}, \tag{A2}$$

where ρ_{D1}, P_{D1}, U_{sD1}, and U_{pD1} are the deuterium density, pressure, shock speed, and particle speed of the incident shock and ρ_{D0} is the initial density. The initial pressure is small and thus neglected as usual. For the deuterium reshock state,

$$\rho_{D2}(U_{sD2} - U_{pD2}) = \rho_{D1}(U_{sD2} - U_{pD1}), \tag{A3}$$

$$P_{D2} - P_{D1} = \rho_{D1}(U_{sD2} - U_{pD1})(U_{pD2} - U_{pD1}), \tag{A4}$$

where ρ_{D2}, P_{D2}, U_{sD2}, and U_{pD2} are the density, pressure, shock speed, and particle speed in the reshock state. Since the quartz Hugoniot has been determined,[75] measurement of U_{sQ} gives $P_{D2}=P_Q$ and $U_{pD2}=U_{pQ}$ in deuterium.

With the four equations (A1)–(A4) we have five unknowns (ρ_{D1}, P_{D1}, U_{pD1}, U_{sD2}, and ρ_{D2}), along with the three known parameters (U_{sD1}, P_{D2}, and U_{pD2}). The final required equation is derived by combining two equations. The first of these is the Rankine-Hugoniot equation expressing the change in internal energy between primary and secondary shocked states ΔE_{21} as

$$\Delta E_{21} = \frac{1}{2}(P_{D2} + P_{D1})\left(\frac{1}{\rho_{D1}} - \frac{1}{\rho_{D2}}\right). \tag{A5}$$

The second equation relates the energy difference ΔE_{21} to P_{D1}, P_{D2}, ρ_{D1} and ρ_{D2} via the material EOS, as given by the constituent relation $E=E(\rho,P)$. In general this is an integral expression involving two independent thermodynamic derivatives, typically the Gruneisen parameter $\Gamma=V(\partial P/\partial E)_V$ and the adiabatic exponent $\gamma=-(\partial \ln P/\partial \ln V)_s$. Since these nondimensional parameters are slowly varying the expression can be simplified to

$$\Delta E_{21} = (P_{D2}/\rho_{D2} - P_{D1}/\rho_{D1})/(\tilde{\gamma} - 1), \tag{A6}$$

where $\tilde{\gamma}$ is an effective adiabatic exponent which quantifies the second-shock compressibility. In the case where the second-shock Hugoniot is on an isentrope and γ is constant, $\tilde{\gamma}$ can be replaced with γ and the equation is exact. If the second-shock Hugoniot is not on an isentrope, this equation is still exact if $\Gamma=\gamma-1$. Given that a second shock in deuterium is actually rather close to both these cases it is quite reasonable to assume the form given in Eq. (A6). Ultimately though, $\tilde{\gamma}$ will be *defined* by Eq. (A6) and computed using models; how close $\tilde{\gamma}$ is to a physical γ is instructive but does not affect the accuracy of the analysis.

Eliminating ΔE_{21} from Eqs. (A5) and (A6) gives

$$\frac{\rho_{D2}}{\rho_{D1}} = 1 + \frac{P_{D2} - P_{D1}}{P_{D1} + (\tilde{\gamma} - 1)(P_{D2} + P_{D1})/2}. \tag{A7}$$

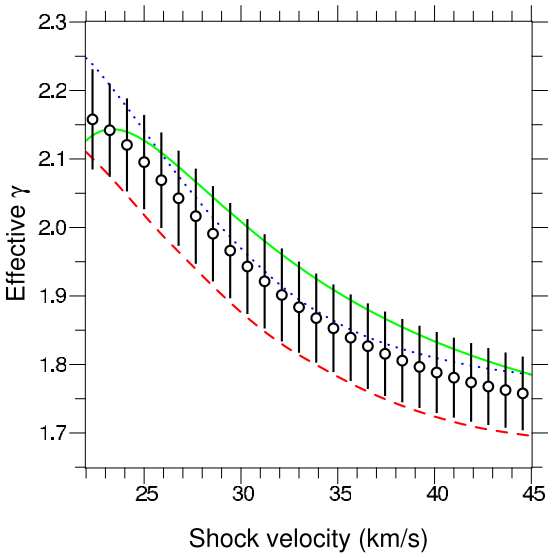

FIG. 13. (Color online) The effective adiabatic exponent $\tilde{\gamma}$ as determined from Eq. (A6) for various D_2 EOS models [Ross (solid green), Sesame72 (dashed red), and Kerley03 (dotted blue)] versus single shock velocity in D_2 (an experimental observable). At very high temperatures, or in the limit of a degenerate electron gas, $\tilde{\gamma}$ should tend toward 5/3. Note that all models appear to give similar values for $\tilde{\gamma}$, demonstrating that second-shock compressibilities are very similar for stiff and soft models. Single shock densities are inferred from double shock measurements by using the model-averaged $\tilde{\gamma}$ shown with open circles; errors in $\tilde{\gamma}$, given by the standard deviation between models, are propagated in the inversion analysis.

It is then an algebraic exercise to solve Eqs. (A1)–(A4) and (A7) for any one of the single shock parameters P_{D1}, ρ_{D1}, or U_{pD1}. In particular, P_{D1} is given by the real root of the implicit cubic equation

$$(P_{D2} - P_{D1})^2\left[1 - \frac{P_{D1}}{\rho_{D0}U_{sD1}^2}\right] = \rho_{D0}\left[P_{D1} + (\tilde{\gamma} - 1)\frac{(P_{D2} + P_{D1})}{2}\right]\left[U_{pD2} - \frac{P_{D1}}{\rho_{D0}U_{sD1}}\right]^2. \tag{A8}$$

Having determined P_{D1}, the density ρ_{D1} can be determined explicitly from Eqs. (A1) and (A2).

Before proceeding with this calculation the effective adiabatic exponent $\tilde{\gamma}$ and its uncertainty must be determined. This was done by examining predictions from several EOS models: Sesame72,[8] the 2003 Kerley model,[34] and the Ross model.[10] By computing pairs of incident (P_{D1},E_{D1},ρ_{D1}) and reflected (P_{D2},E_{D2},ρ_{D2}) shock states for a series of incident shocks in D_2 impacting the quartz anvil, $\tilde{\gamma}$ was calculated directly from Eq. (A6). The results are plotted as a function of U_{sD1} (an experimental observable) and shown in Fig. 13. The fact that $\tilde{\gamma}$ is very similar for all of these models, whether they are stiff or soft, indicates that uncertainties in the second-shock compressibility are quite small, at least to the extent that differences between these models are good predictors of uncertainties. The circular symbols shown in

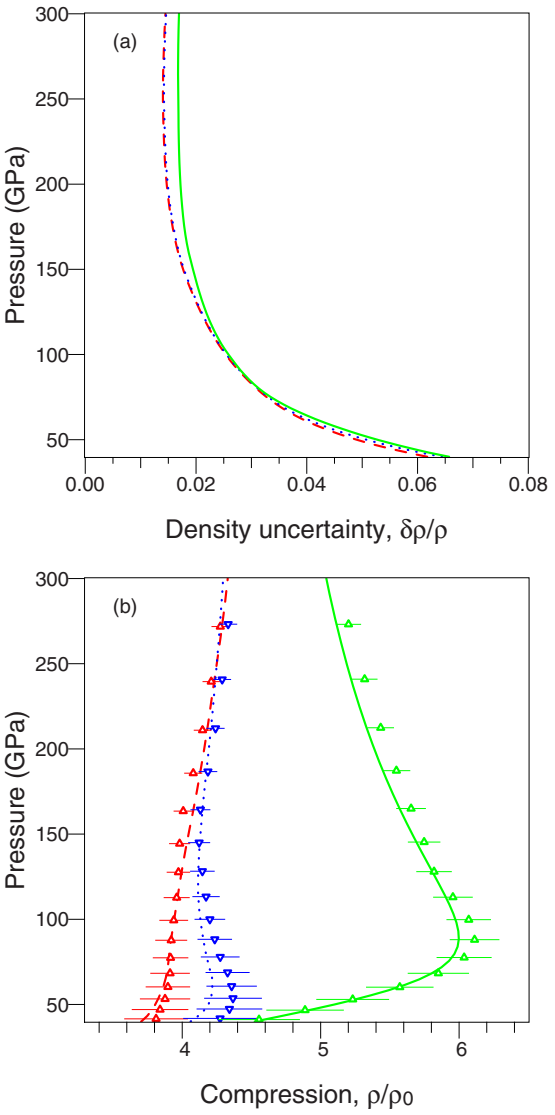

FIG. 14. (Color online) (a) The estimated systematic uncertainty in the first-shock densities which were derived from the double shock inversion analysis; (b) Single shock states inferred from model-calculated double shock states using the $\tilde{\gamma}$ of Fig. 13 (open triangles); error bars show the estimated systematic uncertainty contribution. These are compared to the exact single shock compression curves from Sesame72 (dashed red curve), Kerley03 (dotted blue curve), and Ross EOS (solid green) models. The agreement between the single shock states inferred by the model-averaged inversion analysis and the exact single shock states is apparent.

Fig. 13 represent the average $\tilde{\gamma}(U_{sD1})$ from the three models; the error bars show the standard deviation of the average. This model-averaged $\tilde{\gamma}(U_{sD1})$ can then be used in Eq. (A8) as an estimate of the correct value of $\tilde{\gamma}$ needed to invert the reflected shock states.

Both random and systematic uncertainties are propagated through the analysis in order to produce error estimates for the inverted single shock parameters. Two systematic uncertainties contribute to the inversion process: one is the uncertainty in $\tilde{\gamma}(U_{sD1})$, which can be represented by σ_γ (error bars in Fig. 13), and the second is the uncertainty in the quartz Hugoniot (which translates to uncertainties in P_{D2} and U_{pD2}).

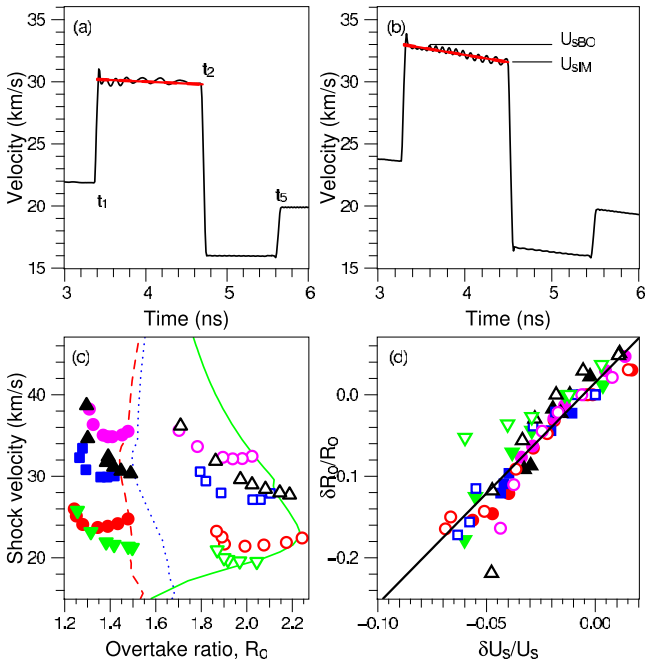

FIG. 15. (Color online) Deviations of shock wave overtake ratios for different degrees of shock unsteadiness as determined by hydrodynamic simulations. Sample shock velocity history in deuterium and quartz for (a) a steady shock and (b) a decaying shock. (c) The expected overtake ratios R_O for steady shocks are shown for three different models: Sesame72 (dashed red curve), Kerley03 (dotted blue curve), and Ross (solid green curve). Hydrodynamic simulations using Sesame72 (solid points) and Ross (open points) illustrate how the measured R_O can drift significantly from the ideal (steady) shock case given by the lines. (d) Scaling of the overtake ratio with the degree of unsteadiness follows an approximately linear relation, independent of EOS model. This linear relation can be used to correct the measured overtake ratio if the shock velocity is monotonically changing by up to 6%–7% over the first-shock transit time.

Figure 14(a) shows the magnitude of the systematic contribution to the relative density (or compression) uncertainty; evidently Eq. (A8) with the model-averaged $\tilde{\gamma}(U_{sD1})$ can be used to invert the incident shock states using the reflected shock data with systematic uncertainty $<4\%$ in density for all three models (stiff or soft) at incident shock Hugoniot pressures >100 GPa.

To test the accuracy of this inversion technique we use the model-averaged $\tilde{\gamma}(U_{sD1})$ described above to invert the observables U_{sD1} and U_{sQ} predicted by each model; the resulting P_{D1} and ρ_{D1} are then compared to the actual single shock values for that model. This also provides a check of the estimated uncertainties in the analysis. The results from this inversion test, as applied to each model, are plotted as the small open symbols shown in Fig. 14(b) and are seen to compare well with the actual single shock Hugoniot values (solid curves in Fig. 13). The error bars in Fig. 14(b) represent the magnitude of the estimated systematic uncertainty propagated through the inversion procedure; it is apparent that the true single shock Hugoniot is captured within the estimated uncertainty band in nearly all cases. This shows that the inversion procedure produces accurate estimates for

the single shock density for models spanning the full range of likely deuterium compressibilities.

APPENDIX B: UNSTEADINESS CORRECTIONS TO MULTISHOCK REVERBERATION TIMES

The technique of using shock reverberation times as a measure of the first-shock compression is particularly susceptible to shock unsteadiness effects. Since the shock velocities in our experiments typically decay slightly with time, it is important to understand the relationship of the overtake ratio R_O to such velocity variations and to establish a means of correcting for them. Here we derive the correction relation for monotonically varying shock velocities.

Several dozen hydrodynamic simulations of the reverberating wave were performed for varying degrees of shock unsteadiness. Nonsteady conditions were created by applying ramped pressure pulses to the target (both positive and negative ramps). Two examples, one for a steady shock and the other for a decaying shock, are shown in Figs. 15(a) and 15(b). For each simulation we obtained the shock velocities at breakout ($U_{s\mathrm{BO}}$) and impact ($U_{s\mathrm{IM}}$) and computed R_O from the various event times; $R_O=(t_2-t_1)/(t_5-t_2)$. The measure of unsteadiness is given by $\delta U_s/U_s=(U_{s\mathrm{IM}}-U_{s\mathrm{BO}})/\langle U_s\rangle$, where $\langle U_s\rangle$ is the average shock velocity in the deuterium.

Figure 15(c) shows how the measured R_O can vary for different degrees of unsteadiness for simulations with two models: the Sesame72 EOS (solid symbols) and Ross EOS (open symbols). These unsteady overtake ratios R_{OU} given by the various points can lie far off the expected R_O for a steady shock, as given by the lines. In particular, attenuating shocks tend to produce a R_{OU} that is *smaller* than the steady shock R_O, making the deuterium EOS appear artificially stiff.

For each nonsteady case we can define the deviation from the ideal case, $\delta R_O=R_{\mathrm{OU}}-R_O$ (here R_O corresponds to the ideal case). Figure 15(d) shows these same simulation data plotted as $\delta R_O/R_O$ versus $\delta U_s/U_s$; this representation reveals a simple empirical relationship $\delta R_O/R_O=2.72\,\delta U_s/U_s$, which appears to be valid over a wide range of shock strengths and is independent of the stiffness of the EOS model (Sesame72 or Ross).

Experimentally observed overtake ratios R_{OM} can thus be adjusted to a corrected overtake ratio R_{OC} using the expression

$$R_{\mathrm{OC}}=R_{\mathrm{OM}}(1+\delta R_O/R_O)^{-1}=R_{\mathrm{OM}}(1+2.72\,\delta U_s/U_s)^{-1}.$$

Aside from the correction coefficient, all the terms on the right-hand side of this equation are observables which can be extracted directly from the data. Note that for slightly decaying shocks $\delta U_s/U_s<0$, so that $R_{\mathrm{OC}}>R_{\mathrm{OM}}$. For most of our data the magnitude of $\delta U_s/U_s$ was less than 0.05.

*Author to whom correspondence should be addressed; hicks13@llnl.gov

†Also at Department of Physics and Astronomy and Department of Mechanical Engineering, University of Rochester, New York, USA.

[1] E. Wigner and H. B. Huntington, J. Chem. Phys. **3**, 764 (1935).
[2] P. Loubeyre, F. Occelli, and R. LeToullec, Nature (London) **416**, 613 (2002).
[3] W. J. Nellis, S. T. Weir, and A. C. Mitchell, Phys. Rev. B **59**, 3434 (1999).
[4] P. M. Celliers, G. W. Collins, L. B. Da Silva, D. M. Gold, R. Cauble, R. J. Wallace, M. E. Foord, and B. A. Hammel, Phys. Rev. Lett. **84**, 5564 (2000).
[5] D. Saumon and T. Guillot, Astrophys. J. **609**, 1170 (2004).
[6] W. B. Hubbard, Nature (London) **431**, 32 (2004).
[7] Because of its higher density, high-shock pressures can more readily be achieved in deuterium than in hydrogen; thus, experiments and hence theories have concentrated on studying the compressibility of deuterium.
[8] G. I. Kerley, Phys. Earth Planet. Inter. **6**, 78 (1972).
[9] D. Saumon and G. Chabrier, Phys. Rev. A **46**, 2084 (1992).
[10] M. Ross, Phys. Rev. B **58**, 669 (1998).
[11] F. J. Rogers, Contrib. Plasma Phys. **41**, 179 (2001).
[12] H. Juranek, R. Redmer, and Y. Rosenfeld, J. Chem. Phys. **117**, 1768 (2002).
[13] T. J. Lenosky, J. D. Kress, and L. A. Collins, Phys. Rev. B **56**, 5164 (1997).
[14] L. Collins, I. Kwon, J. Kress, N. Troullier, and D. Lynch, Phys. Rev. E **52**, 6202 (1995).
[15] T. J. Lenosky, S. R. Bickham, J. D. Kress, and L. A. Collins, Phys. Rev. B **61**, 1 (2000).
[16] L. A. Collins, S. R. Bickham, J. D. Kress, S. Mazevet, T. J. Lenosky, N. J. Troullier, and W. Windl, Phys. Rev. B **63**, 184110 (2001).
[17] M. P. Desjarlais, Phys. Rev. B **68**, 064204 (2003).
[18] S. A. Bonev, B. Militzer, and G. Galli, Phys. Rev. B **69**, 014101 (2004).
[19] W. R. Magro, D. M. Ceperley, C. Pierleoni, and B. Bernu, Phys. Rev. Lett. **76**, 1240 (1996).
[20] B. Militzer and D. M. Ceperley, Phys. Rev. Lett. **85**, 1890 (2000).
[21] V. Bezkrovniy, V. S. Filinov, D. Kremp, M. Bonitz, M. Schlanges, W. D. Kraeft, P. R. Levashov, and V. E. Fortov, Phys. Rev. E **70**, 057401 (2004).
[22] V. S. Filinov, P. R. Levashov, M. Bonitz, and V. E. Fortov, Plasma Phys. Rep. **31**, 700 (2005).
[23] L. B. Da Silva *et al.*, Phys. Rev. Lett. **78**, 483 (1997).
[24] G. W. Collins, L. B. Da Silva, P. Celliers, D. M. Gold, M. E. Foord, R. J. Wallace, A. Ng, S. V. Weber, K. S. Budil, and R. Cauble, Science **281**, 1178 (1998).
[25] G. W. Collins *et al.*, Phys. Plasmas **5**, 1864 (1998).
[26] M. D. Knudson, D. L. Hanson, J. E. Bailey, C. A. Hall, J. R. Asay, and W. W. Anderson, Phys. Rev. Lett. **87**, 225501 (2001).
[27] M. D. Knudson, D. L. Hanson, J. E. Bailey, C. A. Hall, J. R. Asay, and C. Deeney, Phys. Rev. B **69**, 144209 (2004).
[28] S. I. Belov *et al.*, JETP Lett. **76**, 433 (2002).
[29] G. V. Boriskov, A. I. Bykov, R. I. Il'kaev, V. D. Selemir, G. V. Simakov, R. F. Trunin, V. D. Urlin, V. E. Fortov, and A. N.

Shuikin, Dokl. Phys. **48**, 553 (2003).
[30] S. K. Grishechkin *et al.*, JETP Lett. **80**, 398 (2004).
[31] G. V. Boriskov, A. I. Bykov, R. I. Il'kaev, V. D. Selemir, G. V. Simakov, R. F. Trunin, V. D. Urlin, A. N. Shuikin, and W. J. Nellis, Phys. Rev. B **71**, 092104 (2005).
[32] T. R. Boehly *et al.*, Phys. Plasmas **11**, L49 (2004).
[33] N. C. Holmes, M. Ross, and W. J. Nellis, Phys. Rev. B **52**, 15835 (1995).
[34] G. I. Kerley, Sandia National Laboratory, Technical Report No. SAND2003-3613, 2003 (unpublished).
[35] W. J. Nellis, A. C. Mitchell, M. van Thiel, G. J. Devine, R. J. Trainor, and N. Brown, J. Chem. Phys. **79**, 1480 (1983).
[36] J. T. Su and W. A. Goddard, Phys. Rev. Lett. **99**, 185003 (2007).
[37] M. van Thiel, M. Ross, B. L. Hord, A. C. Mitchell, W. H. Gust, M. J. D'Addario, R. N. Keeler, and K. Boutwell, Phys. Rev. Lett. **31**, 979 (1973).
[38] R. D. Dick and G. I. Kerley, J. Chem. Phys. **73**, 5264 (1980).
[39] M. D. Knudson, R. W. Lemke, D. B. Hayes, C. A. Hall, C. Deeney, and J. R. Asay, J. Appl. Phys. **94**, 4420 (2003).
[40] M. D. Knudson, J. R. Asay, and C. Deeney, J. Appl. Phys. **97**, 073514 (2005).
[41] An ambiguity exists in how Boriskov *et al.* (Ref. 31) corrected for the higher initial density of two previous data points (Refs. 28 and 29) on solid deuterium. They state that "since two points were measured with solid samples, shock velocities of these two points were corrected downward by 1.5% to account for their higher initial density relative to that of the liquid samples." (See p. 092104-2, third paragraph, Ref. 31). However, they tabulated these shifted shock velocities as $U_{sD}=20.51$ and 28.64 km/s, which is an upward shift from the values of $U_{sD}=20.3$ and 28.2 km/s originally reported in Ref. 28 and Ref. 29, respectively. The upward shift results in (8–10)% less compression than does the downward shift. Our analysis shown in Sec. IV B indicates that the velocity shift should be downward, as Boriskov *et al.* (Ref. 31) state in their text.
[42] A. N. Mostovych, Y. Chan, T. Lehecha, A. Schmitt, and J. D. Sethian, Phys. Rev. Lett. **85**, 3870 (2000).
[43] A. N. Mostovych, Y. Chan, T. Lehecha, L. Phillips, A. Schmitt, and J. D. Sethian, Phys. Plasmas **8**, 2281 (2001).
[44] M. D. Knudson, D. L. Hanson, J. E. Bailey, C. A. Hall, and J. R. Asay, Phys. Rev. Lett. **90**, 035505 (2003).
[45] T. R. Boehly *et al.*, Opt. Commun. **133**, 495 (1997).
[46] P. C. Souers, *Hydrogen Properties for Fusion Energy* (University of California Press, Berkeley, CA, 1986).
[47] Small changes in the properties of aluminum occur at cryogenic temperatures, the most important of which is the 1.1% increase in density to 2.74 g/cm^3. The Al Hugoniot shifts very slightly, an effect that was taken into account in the impedance-matching analysis by averaging the predicted shift from five different Al EOS tables. Over the entire range under study the change in U_s for a given U_p is $<0.4\%$. The effects on quartz, with its low thermal expansivity, are even smaller. The quartz density was estimated to change by $<0.5\%$ and the refractive index by 0.1% when cooled to <20 K. The predicted shift in the aluminum-to-quartz experimentally defined velocity fit was found to be $<0.15\%$.
[48] L. M. Barker and R. E. Hollenbach, J. Appl. Phys. **43**, 4669 (1972).
[49] L. M. Barker and K. W. Schuler, J. Appl. Phys. **45**, 3692 (1974).
[50] P. M. Celliers, G. W. Collins, L. B. D. Silva, D. M. Gold, and R. Cauble, Appl. Phys. Lett. **73**, 1320 (1998).
[51] P. M. Celliers, D. K. Bradley, G. W. Collins, D. G. Hicks, T. R. Boehly, and W. J. Armstrong, Rev. Sci. Instrum. **75**, 4916 (2004).
[52] D. G. Hicks, T. R. Boehly, J. H. Eggert, J. E. Miller, P. M. Celliers, and G. W. Collins, Phys. Rev. Lett. **97**, 025502 (2006).
[53] D. G. Hicks, T. R. Boehly, P. M. Celliers, J. H. Eggert, E. Vianello, D. D. Meyerhofer, and G. W. Collins, Phys. Plasmas **12**, 082702 (2005).
[54] J. M. Walsh, M. H. Rice, R. G. McQueen, and F. L. Yarger, Phys. Rev. **108**, 196 (1957).
[55] Y. B. Zeldovich and Y. P. Raizer, *Physics of Shock Waves and High Temperature Hydrodynamic Phenomena* (Dover, Mineola, NY, 2002).
[56] P. M. Celliers, G. W. Collins, D. G. Hicks, and J. H. Eggert, J. Appl. Phys. **98**, 113529 (2005).
[57] W. J. Nellis and A. C. Mitchell, J. Chem. Phys. **73**, 6137 (1980).
[58] L. V. Al'tshuler, S. B. Kormer, A. A. Bakanova, and R. F. Trunin, Sov. Phys. JETP **11**, 573 (1960).
[59] A. C. Mitchell and W. J. Nellis, J. Appl. Phys. **52**, 3363 (1981).
[60] V. A. Simonenko, N. P. Voloshin, A. S. Vladimirov, A. P. Nagibin, V. N. Nogin, V. A. Popov, V. A. Vasilenko, and Y. A. Shoĭdin, Sov. Phys. JETP **61**, 869 (1985).
[61] M. A. Podurets, V. M. Ktitorov, R. F. Trunin, L. V. Popov, A. Y. Matveev, B. V. Pechenkin, and A. G. Sevast'yanov, High Temp. **32**, 890 (1994).
[62] M. D. Knudson (private communication).
[63] R. F. Trunin, M. A. Podurets, G. V. Simakov, L. V. Popov, and A. G. Sevast'yanov, JETP **81**, 464 (1995).
[64] G. I. Kerley, Int. J. Impact Eng. **5**, 441 (1987).
[65] S. P. Lyon and J. Johnson, Los Alamos National Laboratory, Technical Report No. LA-CP-98–100, 1998 (unpublished).
[66] R. M. More, K. H. Warren, D. A. Young, and G. B. Zimmerman, Phys. Fluids **31**, 3059 (1988).
[67] N. C. Holmes, in *High-Pressure Science and Technology—1993*, edited by S. C. Schmidt, J. W. Shaner, G. A. Samara, and M. Ross (AIP, New York, 1994), Vol. 309, pp. 153–156.
[68] In many of the Knudson *et al.* experiments the Al flyer plate was shocked during the initial stages of acceleration causing it to strike the target package with a reduced density; this situation was taken into account to infer the Al shock state accurately. Details of this correction are given in Ref. 27.
[69] W. J. Nellis, Phys. Rev. Lett. **89**, 165502 (2002).
[70] V. S. Filinov, V. E. Fortov, M. Bonitz, and P. R. Levashov, JETP Lett. **74**, 384 (2001).
[71] S. Scandolo, Proc. Natl. Acad. Sci. U.S.A. **100**, 3051 (2003).
[72] S. A. Bonev, E. Schwegler, T. Ogitsu, and G. Galli, Nature (London) **431**, 669 (2004).
[73] V. E. Fortov *et al.*, Phys. Rev. Lett. **99**, 185001 (2007).
[74] H. E. Stanley, *Introduction to Phase Transitions and Critical Phenomena* (Oxford University Press, New York, Oxford, 1971).
[75] The quartz Hugoniot is given by $U_p=C_0+C_1(U_s-\alpha)$, where $C_0=12.742\pm0.093$, $C_1=0.775\pm0.021$, and $\alpha=20.574$.